Auto-ejection of liquid from a nozzle

Fang Shan [●],[1] Zhenhua Chai [●],[1,2,3,*] and Baochang Shi [●][1,2,3]

[1]*School of Mathematics and Statistics, Huazhong University of Science and Technology, Wuhan 430074, China*
[2]*Hubei Key Laboratory of Engineering Modeling and Scientific Computing, Huazhong University of Science and Technology,*
Wuhan 430074, China
[3]*Institute of Interdisciplinary Research for Mathematics and Applied Science, Huazhong University of Science and Technology,*
Wuhan 430074, China

Auto-ejection of liquid is an important process in engineering applications, and is also very complicated since it involves interface moving, deforming, and jet breaking up. In this work, a theoretical velocity of meniscus at nozzle exit is first derived, which can be used to analyze the critical condition for auto-ejection of liquid. Then a consistent and conservative axisymmetric lattice Boltzmann (LB) method is proposed to study the auto-ejection process of liquid jet from a nozzle. We test the LB model by conducting some simulations, and find that the numerical results agree well with the theoretical and experimental data. We further consider the effects of contraction ratio, length ratio, contact angle, and nozzle structure on the auto-ejection, and observe some distinct phenomena during the ejection process, including the deformation of meniscus, capillary necking, and droplet pinch off. Finally, the results reported in the present work may play an instructive role on the design of droplet ejectors and the understanding of jetting dynamics in microgravity environment.

I. INTRODUCTION

The auto-ejection process has some fundamental applications in engineering and biological fields, such as ink-jet printing [1], molten microdrops technology [2], and biochip arrayers [3]. Basically, however, this process is caused by the capillary rise that mainly depends on the capillary geometry, fluid properties, and fluid-solid interaction [4].

Up to now, there are many theoretical and experimental studies that have been carried out on the capillary rising problems. A century ago, Lucas [5] considered the effect of viscous force, and obtained a theoretical solution of meniscus. In 1921, Washburn [6] studied the rate of penetration into a capillary tube, and derived the rising height of meniscus in time once the gravity is neglected,

$$z = \sqrt{\frac{R\sigma\cos\theta}{2\mu_l}t}, \qquad (1)$$

which is termed as the classical Lucas-Washburn equation. z is the penetration height, R is the tube radius, σ is the surface tension coefficient, θ is the contact angle, and μ_l is the viscosity of liquid. It should be noted that during initial rising time, the inertial force is dominant, and the capillary rising dynamics at this stage can be described by Ref. [7]

$$z = t\sqrt{\frac{2\sigma\cos\theta}{R\rho_l}}, \qquad (2)$$

where ρ_l is the density of liquid. Bosanquet [8] first took the effects of inertial and viscous forces into account, and

obtained a theoretical solution of meniscus height,

$$z = \sqrt{\frac{R\sigma\cos\theta}{2\mu_l}\left[t - \frac{R^2\rho_l}{8\mu_l}\left(1 - e^{-\frac{8\mu_l}{R^2\rho_l}t}\right)\right]}. \qquad (3)$$

With more liquid rising into the tube, however, the effect of gravitational force becomes more significant. To consider the influence of gravity, Fries and Dreyer [9] presented a momentum balance equation in which the gravitational force, viscous force, and inertial force of the liquid column are included,

$$\frac{2\sigma\cos\theta}{R} = \frac{d(\rho_l z\dot{z})}{dt} + \frac{8\mu_l z\dot{z}}{R^2} + \rho_l gz, \qquad (4)$$

where $\dot{z}$ is the rising velocity of meniscus. Furthermore, they also derived the analytical solutions under different time stages (inertial stage, viscous stage, and gravitational stage).

In addition, some available works also demonstrated that the displaced gas or liquid also has a remarkable effect on the capillary rising process. For instance, Hultmark *et al.* [10] investigated the viscous effect of displaced gas on the imbibition process of liquid theoretically and experimentally, and derived a theoretical solution of the meniscus height,

$$z = \sqrt{\frac{R\sigma\cos\theta}{2\mu_l}t + \left(\frac{\mu_g L}{\mu_l}\right)^2} - \frac{\mu_g L}{\mu_l}, \qquad (5)$$

where μ_g is the viscosity of the gas and L is the length of tube. On the other hand, Walls *et al.* [11] studied the influences of gravitational and viscous forces of the displaced fluids on the capillary displacement, and also obtained some simplified governing equations and the analytical solutions under different limiting cases. Recently, Shan *et al.* [12] further extended the previous works [9–11] to

the capillary rise of non-Newtonian power-law fluids, and also presented the theoretical solutions of some different cases.

It should be noted that the meniscus may oscillate around the Jurin's height ($z = \frac{2\sigma \cos\theta}{\Delta \rho g R}$) [13] in the capillary rising process, and some works are performed on critical conditions and mechanisms for the oscillation. For example, Quéré *et al.* [14] analyzed the criterion, shape, and damping of oscillation through introducing a dimensionless parameter $\Omega = 8\sqrt{2}\sigma \mu_l R^{-5/2} \rho_l^{-3/2}$, and obtained the critical value $\Omega = 2$. From the viewpoint of energy conversion, Shardt *et al.* [15] studied the meniscus inverting and spreading onto the top surface of the tube, and found that the occurrence of oscillation is determined by the ratio of the kinetic energy and surface energy, which can be denoted by Weber number (We = $\rho_l z \dot{z}^2 / 8\sigma$). Combining the experimental and theoretical analysis, Marston *et al.* [16] conducted a study on the oscillation behavior of meniscus in a cylindrical tube where the effects of the rebound height, immersion depth, tube radius, and fluid properties are considered. They also gave a critical condition theoretically, and demonstrated that it is consistent with the experimental observation. Das and Mitra [17] performed an analysis on the characteristics of oscillation, and illustrated that the different regimes in a vertical capillary filling are determined by the Ohnesorge number (Oh = $\mu / \sqrt{\rho R \sigma}$) and Bond number (Bo = $\rho g R^2 / \sigma$), and also, the transition from inertial regime to oscillatory regime was identified. Lorenceau *et al.* [18] proposed a model to depict the gravity oscillation and long-range damping of a liquid column, and demonstrated that the theoretical solution is dependent on the liquid viscosity. Additionally, they also found that the oscillation trajectory is parabolic.

We would also like to point out that during the capillary rise of liquid in a cylindrical tube, the liquid could never expel itself from the tube even when the tube length is less than the equilibrium height [19], and the meniscus would oscillate around the tube exit until it reaches an equilibrium state [20], which is caused by the combined effects of pinning at sharp edge, kinetic energy, and surface energy. To enforce the liquid to rush out from the tube, it would have to form a state of overpressure, and an inverted meniscus is produced. Actually, it has been known that the dynamic behavior of meniscus can be changed through altering the geometry of tube, and the large inertia may be induced in a nozzle to overcome surface tension enabling the ejection of droplets automatically. Wollman *et al.* [19,21,22] conducted the capillarity-driven droplet ejection experiments on the drop towers. In their works, a force balance model is proposed to predict the velocity of the meniscus, and a criteria for capillarity-driven droplet ejection is presented along with details for the data collection, reduction and analysis,

$$\text{We} = \frac{\rho_l R W_t}{12\sigma \alpha^4 (1 + K_n^4)} \geqslant 1, \qquad (6)$$

where W_t is the velocity at inlet of the nozzle, α is the ratio of nozzle radius to capillary radius, and K_n is the loss coefficient ascribed to the nozzle. Mehrabian and Feng [23]

used a diffuse-interface model to study the process of auto-ejection, and developed a criterion to predict the number of ejected droplets under some geometric parameters, which is related to an instantaneous Weber number and an effective tube length. Dong *et al.* [24] studied the drop-on-demand (DOD) drop formation experimentally, and the ejection and stretching of liquid, pinch off of the liquid thread from the nozzle exit were analyzed. In addition, the droplet ejection has some important applications in different fields. In the area of industry, Utada *et al.* [25] used a microcapillary geometry to fabricating double emulsions, which involves the drop dripping and jetting. In the field of electronic packages, Pekkanen *et al.* [26] applied ink-jet technology to manufacture the interconnection patterns for integrated electronics module, where the drop shape, formation, and velocity are controlled accurately. In the aspect of medical diagnostics, Beg *et al.* [27] discussed the three-dimensional (3D)-printing technology to manufacture drug delivery systems, which have the ability to design customized drug products with high flexibility for selecting the dose, shape, and size of the dosage form to meet patient needs. Different from above works, here we pay attention to the dynamic behavior when the liquid reaches the end of nozzle from a numerical point of view. It is known that the ejection process is influenced significantly by the geometry of the nozzle, and what is more, the meniscus acceleration process inside the nozzle and the mechanism of auto-ejection have not been well understood. In this work, we will conduct a comprehensive study on auto-ejection of liquid from a nozzle. The rest of the paper is organized as follows. In Sec. II, we first present a theoretical expression of contact-line velocity at the end of nozzle, and then obtain a critical condition for auto-ejection process. In Sec. III, we develop a consistent and conservative axisymmetric lattice Boltzmann (LB) method to investigate the ejection process, and also provide some details on how to implement the wetting boundary conditions on curved surface. In Sec. IV, a benchmark problem of droplet spreading on a solid sphere, and a comparison between numerical and experimental results of the auto-ejection are used to validate the developed LB method. In Sec. V, we investigate the auto-ejection process where the effects of geometry of the nozzle and contact angle are considered, and also conduct an analysis on the jet breakup process. Finally, some conclusions are summarized in Sec. VI.

II. A THEORETICAL ANALYSIS ON THE AUTO-EJECTION OF LIQUID FROM THE NOZZLE

The auto-ejection of liquid refers to the process where the liquid rushes out from the nozzle exit and forms a liquid column under the influences of capillary force and gravitational force. The axisymmetric geometry of the problem consists of a capillary tube, which connects to the liquid at the bottom and air at the top (see Fig. 1). The tube has a contracting nozzle at its top end where the radius shrinks from R_b to R_t at the end of the nozzle, the nozzle angle is α, the total length is $L = L_b + L_t$ with L_b and L_t being the lengths of the tube and the nozzle. In this section, we will focus on how to derive the meniscus velocity and critical condition for auto-ejection of liquid jet from the nozzle.

FIG. 1. Schematic of auto-ejection and boundary conditions.

A. Meniscus velocity at the end of nozzle

According to the previous works [28–30], the velocity of the problem can be approximated by the Hagen-Poiseuille law,

$$v(r) = \frac{1}{4\mu_l}\left(\frac{\partial p}{\partial z} + \rho_l g\right)[r^2 - R(z)^2], \tag{7}$$

where r denotes the axial coordinate in cylindric coordinates, g is the gravitational acceleration, and p is the pressure. From Eq. (7), one can also obtain the volumetric flow rate,

$$Q = -\frac{R^4\pi}{8\mu_l}\left(\frac{\partial p}{\partial z} + \rho_l g\right). \tag{8}$$

For the meniscus at the position $h(z)$, the capillary pressure P_c can be expressed as [31]

$$P_c|_{z=h} = p_n - p_w = \frac{2\sigma\cos(\theta-\alpha)}{R(h)}, \tag{9}$$

where p_n is the pressure in nonwetting phase, p_w is the pressure in wetting phase, and $R(h)$ is related to the position h,

$$R(h) = \begin{cases} R_t + (L_b + L_t - h)\tan\alpha & h > L_b \\ R_b & 0 < h \leqslant L_b. \end{cases} \tag{10}$$

Integrating Eq. (8) from 0 to h with $P_c|_{z=0} = 0$, we have

$$\frac{2\sigma\cos(\theta-\alpha)}{R(h)} - \rho_l gh = 8\mu_l \frac{Q}{\pi}\int_0^h \frac{dz}{R(z)^4}. \tag{11}$$

With the help of mass conservation and $Q = \pi R(h)^2 \frac{dh}{dt}$, Eq. (11) can be rewritten as [28]

$$\int_0^h \frac{dz}{R(z)^4}\frac{dh}{dt} = \frac{\frac{2\sigma\cos(\theta-\alpha)}{R(h)} - \rho_l gh}{8\mu_l R(h)^2}, \tag{12}$$

then substituting Eq. (10) into Eq. (12) yields

$$\left\{\int_0^{L_b}\frac{dz}{R_b^4} + \int_{L_b}^h \frac{dz}{[R_t + (L_b + L_t - z)\tan\alpha]^4}\right\}\frac{dh}{dt}$$

$$= \frac{\frac{2\sigma\cos(\theta-\alpha)}{R(h)} - \rho_l gh}{8\mu_l R(h)^2}. \tag{13}$$

When the contact line first reaches the end of nozzle where $h = L_b + L_t$, the velocity of the meniscus V_t can be obtained,

$$V_t = \frac{\frac{2\sigma\cos(\theta-\alpha)}{R_t} - \rho_l g(L_b + L_t)}{8\mu_l R_t^2\left[\frac{L_b}{R_b^4} + \frac{1}{3\tan\alpha}\left(R_t^{-3} - R_b^{-3}\right)\right]}. \tag{14}$$

B. Critical condition for auto-ejection of liquid jet

As the liquid is coming out from a tube, it would be in a state of overpressure that produces an inverted meniscus. When the kinetic energy is consumed by the liquid pressure, we have

$$\tfrac{1}{2}\rho_l\pi R_t^2\delta h V_t^2 = P_c\pi R_t^2\delta h, \tag{15}$$

taking $P_c = 2\sigma/R_t$, one can obtain

$$\frac{1}{2}\rho_l V_t^2 = \frac{2\sigma}{R_t}. \tag{16}$$

If we denote the velocity of meniscus when wetting fluid ejected from the nozzle as V_e, the decrease of meniscus velocity due to the inversion of the meniscus curvature in terms of dynamics pressure can be given by [19]

$$\frac{\rho_l V_t^2}{2} - \frac{\rho_l V_e^2}{2} = \frac{4\sigma}{R_t}. \tag{17}$$

After the inversion of the meniscus, the liquid has the sufficient inertia to overcome the resistance of the surface tension. Through balancing the inertial force and surface tension force of the fluids [19], we have

$$\frac{\rho_l V_e^2}{2R_t} \sim \frac{2\sigma}{R_t^2}, \tag{18}$$

after rearranging, one can obtain

$$\frac{\rho_l R_t V_e^2}{4\sigma} \geqslant 1. \tag{19}$$

Substituting Eq. (17) into Eq. (19), the necessary condition for auto-ejection phenomenon can be obtained,

$$\frac{\rho_l R_t V_t^2}{12\sigma} \geqslant 1. \tag{20}$$

If we introduce the Weber number defined by We $= \rho_l R_t V_t^2/12\sigma$, the critical condition can be rewritten as

$$\text{We} = 1. \tag{21}$$

Here we would like to point out that unlike the previous works [19,23], the critical condition is mainly dependent on the geometry of the nozzle and the fluid properties, and the velocity V_t can be predicted by Eq. (14) for a specified geometry of the nozzle.

III. MATHEMATICAL MODEL AND NUMERICAL METHOD

To keep consistence with above theoretical analysis, in this section we will first present the axisymmetric mathematical model for the auto-ejection of liquid jet, and then develop a consistent and conservative LB method for the model. Finally, a special discussion on how to treat boundary conditions on the curved surface is also presented.

A. A consistent and conservative mathematical model for axisymmetric two-phase flows

To describe the movement of the interface between different phases and fluid flows, the following conservative Allen-Cahn equation for phase field and consistent incompressible Navier-Stokes equations (NSEs) for fluid field are considered in the cylindrical coordinate,

$$\frac{\partial r\phi}{\partial t} + \nabla \cdot (r\phi\mathbf{u} + M_\phi\phi\mathbf{E}) = \nabla \cdot M_\phi[\nabla(r\phi) - r\lambda\mathbf{n}], \quad (22)$$

$$\nabla \cdot r\mathbf{u} = 0, \quad (23a)$$

$$\frac{\partial(r\rho\mathbf{u})}{\partial t} + \nabla \cdot (r\rho\mathbf{u}\mathbf{u} + \mathbf{m}^\phi\mathbf{u}) = -\nabla(rp) + \nabla \cdot [r\nu\rho(\nabla\mathbf{u} + \nabla\mathbf{u}^\top)] + \mathbf{F}, \quad (23b)$$

$$\mathbf{F} = r(\mathbf{F}_s + \mathbf{G}) + \left(p - \frac{2\rho\nu}{r}\right)\mathbf{E}, \quad (23c)$$

where ϕ is the order parameter, M_ϕ is a positive constant named mobility, $\mathbf{u}$ is the velocity, $\lambda = 4\phi(1 - \phi)/W$ with W being the interface thickness, $\mathbf{E} = (1, 0)$, and $\mathbf{G}$ is the gravitational force. The unit vector normal to the interface $\mathbf{n}$, the surface tension $\mathbf{F}_s$, the mass flux $\mathbf{m}^C$ and mass diffusion $\mathbf{m}^\phi$ are defined by

$$\mathbf{n} = \frac{\nabla\phi}{|\nabla\phi|}, \quad \mathbf{F}_s = \tilde{\mu}_\phi\nabla\phi, \quad (24a)$$

$$\mathbf{m}^C = \rho\mathbf{u} + \mathbf{m}^\phi,$$

$$\mathbf{m}^\phi = \frac{\rho_l - \rho_g}{\phi_l - \phi_g}[M_\phi\phi\mathbf{E} - M_\phi(\nabla(r\phi) - r\lambda\mathbf{n})], \quad (24b)$$

where $\tilde{\mu}_\phi = \mu_\phi - \kappa\partial_r\phi/r$, μ_ϕ is the chemical potential given by

$$\mu_\phi = 4\beta(\phi - \phi_l)(\phi - \phi_g)\left(\phi - \frac{\phi_l + \phi_g}{2}\right) - \kappa\nabla^2\phi. \quad (25)$$

Here $\phi_l = 1.0$ and $\phi_g = 0$ are corresponding to liquid and gas phases, respectively, and the interface is marked by the contour level of $\phi = (\phi_l + \phi_g)/2$. The physical parameters κ and β are dependent on the interface thickness and the surface tension σ,

$$\kappa = \frac{3}{2}\sigma W, \quad \beta = \frac{12\sigma}{W}. \quad (26)$$

Compared to the previous works [20,32,33], the mass diffusion between different phases $\mathbf{m}^\phi$ is introduced into the NSEs, and a consistent mass flux $\mathbf{m}^C$ is redefined. Additionally, it should be noted that the consistent and conservative model composed of Eqs. (22) and (23) can preserve the consistency of mass conservation and momentum transport through including the flux caused by the mass diffusion $\mathbf{m}^\phi$ in the interface layer, and some unphysical phenomena can be eliminated [34,35].

B. Consistent and conservative LB method for axisymmetric mathematical model

1. LB model for conservative Allen-Cahn equation

The evolution equation of the multiple-relaxation-time (MRT-LB) model for the conservative Allen-Cahn equation can be expressed as [36]

$$f_i(\mathbf{x} + \mathbf{c}_i\Delta t, t + \Delta t) - f_i(\mathbf{x}, t)$$
$$= -\Lambda_{ij}[f_j(\mathbf{x}, t) - f_j^{eq}(\mathbf{x}, t)] + \Delta t\left(\delta_{ij} - \frac{\Lambda_{ij}}{2}\right)F_j(\mathbf{x}, t), \quad (27)$$

where $f_i(\mathbf{x}, t)$ is the particle distribution function and $\Lambda_{ij} = (\mathbf{M}^{-1}\mathbf{S}^f\mathbf{M})_{ij}$ is the collision matrix. In the D2Q9 (nine discrete velocities in two-dimensional space) lattice model considered here, the transformation matrix $\mathbf{M}$, the diagonal relaxation matrix $\mathbf{S}^f$, the discrete velocity $\mathbf{c}_i$ and weight coefficient ω_i can be given by

$$\mathbf{M} = \begin{pmatrix} 1 & 1 & 1 & 1 & 1 & 1 & 1 & 1 & 1 \\ -4 & -1 & -1 & -1 & -1 & 2 & 2 & 2 & 2 \\ 4 & -2 & -2 & -2 & -2 & 1 & 1 & 1 & 1 \\ 0 & 1 & 0 & -1 & 0 & 1 & -1 & -1 & 1 \\ 0 & -2 & 0 & 2 & 0 & 1 & -1 & -1 & 1 \\ 0 & 0 & 1 & 0 & -1 & 1 & 1 & -1 & -1 \\ 0 & 0 & -2 & 0 & 2 & 1 & 1 & -1 & -1 \\ 0 & 1 & -1 & 1 & -1 & 0 & 0 & 0 & 0 \\ 0 & 0 & 0 & 0 & 0 & 1 & -1 & 1 & -1 \end{pmatrix}, \quad (28a)$$

$$\mathbf{S}^f = \text{diag}(s_0^f, s_1^f, s_2^f, s_3^f, s_4^f, s_5^f, s_6^f, s_7^f, s_8^f), \quad (0 < s_i^f < 2) \quad (28b)$$
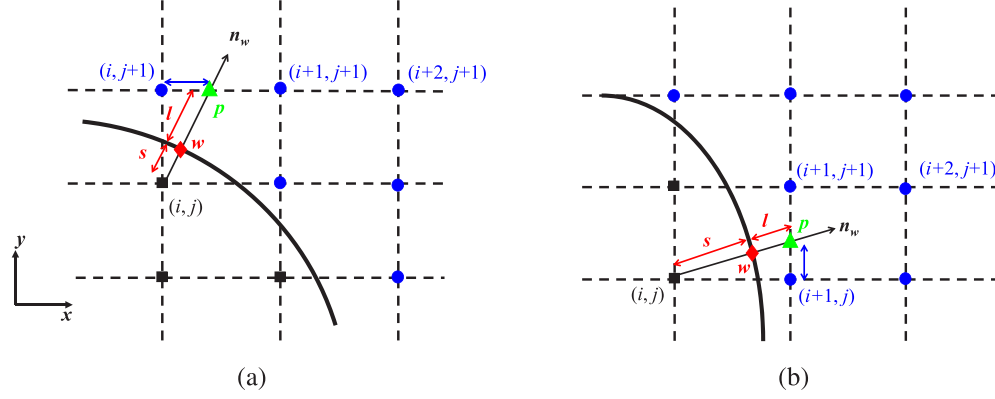
FIG. 2. Schematic of interpolation schemes [fluid nodes (circle dots), solid nodes (square dots), and boundary nodes (diamond dots)].

$$\mathbf{c}_i = \begin{pmatrix} 0 & 1 & 0 & -1 & 0 & 1 & -1 & -1 & 1 \\ 0 & 0 & 1 & 0 & -1 & 1 & 1 & -1 & -1 \end{pmatrix} c,$$

(29a)

$$\omega_i = \begin{pmatrix} \dfrac{4}{9} & \dfrac{1}{9} & \dfrac{1}{9} & \dfrac{1}{9} & \dfrac{1}{9} & \dfrac{1}{36} & \dfrac{1}{36} & \dfrac{1}{36} & \dfrac{1}{36} \end{pmatrix},$$

(29b)

where $c = \Delta x/\Delta t$ is the lattice speed with Δx and Δt representing the grid spacing and time step. For simplicity, Δx and Δt are set as the lattice and time units, i.e., $\Delta x = \Delta t = 1$.

To recover the conservative Allen-Cahn equation correctly (see Appendix A), the following equilibrium distribution function f_k^{eq} and source distribution function F_k are adopted [33],

$$f_j^{\mathrm{eq}} = \omega_j \left[r\phi + \frac{\mathbf{c}_j \cdot (r\phi \mathbf{u} + \phi M_\phi \mathbf{E})}{c_s^2} \right],$$

(30)

$$F_j = \frac{\omega_j \mathbf{c}_j \cdot \left[\partial_t (r\phi \mathbf{u} + \phi M_\phi \mathbf{E}) + c_s^2 r\lambda \mathbf{n} \right]}{c_s^2}.$$

(31)

In addition, the order parameter and the mobility are determined by

$$\phi = \frac{1}{r} \sum_j f_j,$$

(32)

$$M_\phi = c_s^2 (\tau_f - 0.5)\Delta t,$$

(33)

where $\tau_f = 1/s_3^f = 1/s_5^f$. In the following simulations, the other relaxation parameters in the relaxation matrix $\mathbf{S}^f$ are fixed as $s_0^f = s_1^f = s_2^f = s_7^f = s_8^f = 1.0$ and $s_4^f = s_6^f = 1/\tau_f$.

2. LB model for consistent incompressible equations

Here we also consider the MRT-LB model for the Navier-Stokes equations [Eq. (23)], and the evolution equation of the model reads [36]

$$g_i(\mathbf{x} + \mathbf{c}_i \Delta t, t + \Delta t) - g_i(\mathbf{x}, t) = - \Lambda_{ij} \left[g_j(\mathbf{x}, t) - g_j^{\mathrm{eq}}(\mathbf{x}, t) \right]$$

$$+ \Delta t \left(\delta_{ij} - \frac{\Lambda_{ij}}{2} \right) G_j(\mathbf{x}, t).$$

(34)

Here $g_i(\mathbf{x}, t)$ is the distribution function and $\Lambda_{ij} = (\mathbf{M}^{-1}\mathbf{S}^g\mathbf{M})_{ij}$ is the collision matrix. To satisfy the divergence-free condition of velocity, the equilibrium distribution function $g_j^{\mathrm{eq}}(\mathbf{x}, t)$ should be given by

$$g_j^{\mathrm{eq}} = \begin{cases} \dfrac{rp}{c_s^2}(\omega_j - 1) + s_j(r, \rho, \phi, \mathbf{u}), & j = 0 \\[2mm] \dfrac{rp}{c_s^2}\omega_j + s_j(r, \rho, \phi, \mathbf{u}), & j \neq 0 \end{cases}$$

(35)

with

$$s_j(r, \rho, \phi, \mathbf{u})$$
$$= \omega_j \left[\frac{\mathbf{c}_j \cdot (r\rho \mathbf{u})}{c_s^2} + \frac{(r\rho \mathbf{uu} + \mathbf{m}^\phi \mathbf{u}) : (\mathbf{c}_j \mathbf{c}_j - c_s^2 \mathbf{I})}{2c_s^4} \right].$$

(36)

For the axisymmetric flows, the D2Q9 lattice model is still adopted, the weight coefficients ω_j and the discrete velocities $\mathbf{c}_j$ are the same as Eqs. (29a) and (29b). The diagonal relaxation matrix $\mathbf{S}^g$ in Eq. (34) is expressed as

$$\mathbf{S}^g = diag\left(s_0^g, s_1^g, s_2^g, s_3^g, s_4^g, s_5^g, s_6^g, s_7^g, s_8^g \right), (0 < s_j^g < 2).$$

(37)
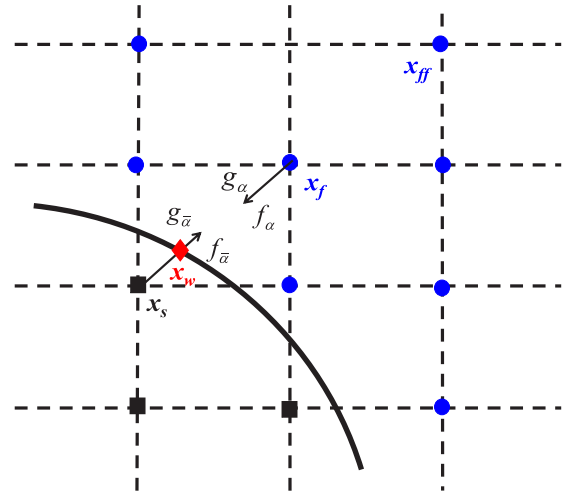
FIG. 3. Schematic of fluid nodes (circle dots), solid nodes (square dots), and boundary nodes (diamond dots) around a curved boundary.
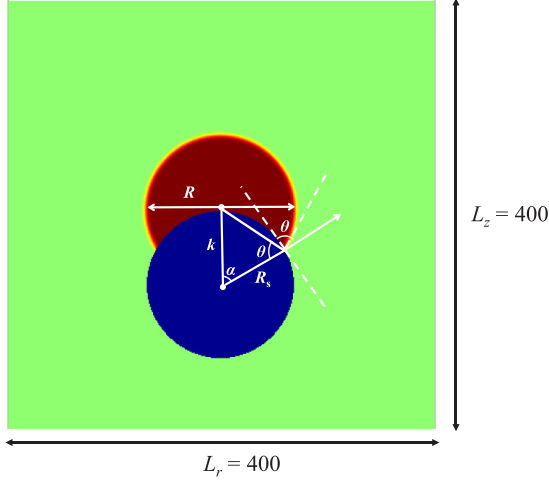
FIG. 4. Schematic of droplet spreading on a solid sphere.

To recover incompressible Navier-Stokes equations (see Appendix B), the force distribution function is designed by

$$
G_j = \omega_j \left[r\mathbf{u} \cdot \nabla \rho + \frac{\mathbf{c}_j \cdot \bar{\mathbf{F}}}{c_s^2} \right.
$$
$$
\left. + \frac{(\mathbf{u}\tilde{\mathbf{F}} + \tilde{\mathbf{F}}\mathbf{u} + \partial_t (\mathbf{m}^\phi \mathbf{u})) : (\mathbf{c}_j \mathbf{c}_j - c_s^2 \mathbf{I})}{2c_s^4} \right], \quad (38)
$$

where $\tilde{\mathbf{F}} = \bar{\mathbf{F}} + c_s^2 \nabla(r\rho)$, and $\bar{\mathbf{F}} = r(\mathbf{F}_s + \mathbf{G}) + (p - \frac{2\rho\nu}{r} u_r)$ $\mathbf{E} + \mathbf{F}^\phi$ with $\mathbf{F}^\phi = -\nabla \cdot (\mathbf{m}^\phi \mathbf{u} - \mathbf{u}\mathbf{m}^\phi)/2$.

The macroscopic fluid velocity is calculated by

$$
r\rho \mathbf{u} = \sum_j \mathbf{c}_j g_j + 0.5\Delta t \bar{\mathbf{F}}, \quad (39)
$$

which can be further recast explicitly as

$$
\mathbf{u} = \frac{\sum_j \mathbf{c}_j g_j + 0.5\Delta t [r(\mathbf{F}_s + \mathbf{G}) + \mathbf{F}^\phi + p\mathbf{I}]}{r\rho + \Delta t r^{-1} \nu \rho \mathbf{E}}. \quad (40)
$$

In addition, it should be noted that the fluid density ρ is taken as a linear function of the order parameter ϕ, and is given by

$$
\rho = \phi(\rho_l - \rho_g) + \rho_g. \quad (41)
$$

The pressure p can be computed by (see Appendix C for details)

$$
p = \frac{c_s^2}{(1 - \omega_0)} \left[\frac{1}{r} \sum_{j \neq 0} g_j + \frac{1}{r} s_0(r, \rho, \phi, \mathbf{u}) + + \frac{\Delta t}{2} \mathbf{u} \cdot \nabla \rho \right.
$$
$$
+ \Delta t \frac{2}{r3c^2} \mathbf{u} \cdot \bar{\mathbf{F}} + \Delta t \frac{2}{9r} s_{p_1} \rho \nu + \Delta t \frac{1}{3c^2 r} s_{p_1} \partial_t (\mathbf{m}^\phi \cdot \mathbf{u})
$$
$$
\left. + \Delta t s_{p_2} r\mathbf{u} \cdot \nabla \rho + \Delta t s_{p_3} \frac{1}{3rc^2} \partial_t (\mathbf{m}^\phi \cdot \mathbf{u}) \right], \quad (42)
$$

where s_{p_1}, s_{p_2} and s_{p_3} are related to the relaxation parameters through $s_{p_1} = \frac{s_1^g s_2^g - s_1^g - s_2^g}{s_1^g s_2^g}$, $s_{p_2} = \frac{s_2^g - s_0^g}{s_0^g s_2^g}$ and $s_{p_3} = \frac{s_1^g + s_2^g}{s_1^g s_2^g}$. In our simulations, the relaxation parameters s_0^g, s_3^g and s_5^g corresponding to the conserved moments are taken as 1.0, while s_7^g and s_8^g related to the kinematic viscosity ν can be determined

by

$$
s_7^g = s_8^g = \frac{1}{\tau_g}, \quad \nu = c_s^2 \left(\tau_g - \frac{1}{2} \right) \Delta t. \quad (43)
$$

The other relaxation parameters are set as $s_1^g = 0.75$, $s_2^g = 0.8$, and $s_4^g = s_6^g = 1.0$.

C. Implementation of boundary conditions on the curved surface

1. Discretization of the wetting boundary condition

To impose a specified contact angle at a solid boundary, the following boundary condition can be applied [37],

$$
\mathbf{n}_w \cdot \nabla \phi \mid_{\mathbf{x}_w} = \Theta \phi_w (1 - \phi_w), \quad (44)
$$

where ϕ_w is the phase-field value at wall boundary, and Θ is related to the contact angle θ,

$$
\Theta = -\sqrt{\frac{2\beta}{\kappa}} \cos\theta. \quad (45)
$$

After discretizing the left-hand-side term of Eq. (44) with the central-difference scheme, one can obtain

$$
\mathbf{n}_w \cdot \nabla \phi \bigg|_{\mathbf{x}_w} = \frac{\partial \phi}{\partial n_w} |_{\mathbf{x}_w} = \frac{\phi_p - \phi_{i,j}}{2l} = \Theta \phi_w (1 - \phi_w), \quad (46)
$$

where ϕ_p is the interpolated phase-field value at the point p [see Fig. 2(a)], $\phi_{i,j}$ is the unknown phase-field value, and $l = |\mathbf{x}_p - \mathbf{x}_w|$ is the distance between the boundary node w and the interpolated point p. To obtain the value of $\phi_{i,j}$, the following scheme is adopted [38],

$$
\phi_{i,j} = \frac{s + l}{2al}(1 + a - \sqrt{(1 + a)^2 - 4a\phi_p}) - \frac{s}{l}\phi_p,
$$
$$
a = l\Theta \neq 0 \ (\theta \neq 90°), \quad (47)
$$

where $s = |\mathbf{x}_w - \mathbf{x}_{i,j}|$ is the distance between the boundary node w and the solid node (i, j), ϕ_p can be calculated by using the unidirectional interpolation. Additionally, if the slope of the vector normal to the boundary is larger than unity [see Fig. 2(a)], the interpolation is carried out in the z direction; otherwise, the interpolation is carried out in the r direction [see Fig. 2(b)].

2. Boundary conditions of the distribution functions

In the implementation of LB method, we must identify the boundary conditions of distribution functions (or unknown distribution functions) from the given physical boundary conditions. On one hand, to determine the unknown phase-field distribution functions at the solid nodes, the halfway bounce-back scheme is adopted (see Fig. 3),

$$
f_{\bar{\alpha}}(\mathbf{x}_s, t + \Delta t) = f_\alpha(\mathbf{x}_f, t + \Delta t), \quad (48)
$$

where $\bar{\alpha}$ is the opposite direction of α, $\mathbf{x}_s$ is solid node near the boundary, $\mathbf{x}_f$ is the fluid node near the boundary. On the other hand, the Yu-Mei-Shyy scheme [39] is used to determine the

TABLE I. The measured values of the contact angle and the relative errors.

Contact angle (deg)	Predicted value (deg)	Relative errors (%)
30°	30.89°	2.99
60°	58.88°	1.86
90°	91.70°	1.92
135°	138.9°	2.89

unknown flow-field distribution functions (see Fig. 3),

$$g_{\bar{\alpha}}(\mathbf{x}_s, t + \Delta t) = \frac{\delta}{1+\delta}[g_{\bar{\alpha}}(\mathbf{x}_f, t + \Delta t) + g_{\alpha}(\mathbf{x}_f, t + \Delta t)]$$
$$+ \frac{1-\delta}{1+\delta}g_{\bar{\alpha}}(\mathbf{x}_{ff}, t + \Delta t), \quad (49)$$

where $\delta = |\mathbf{x}_f - \mathbf{x}_w|/|\mathbf{x}_f - \mathbf{w}_s|$ and $\mathbf{x}_{ff} = (\mathbf{x}_f + \mathbf{c}_\alpha \delta t)$ is the fluid node.

IV. NUMERICAL VALIDATION

In this section, we will test the axisymmetric LB method by considering two benchmark problems. The first one is a droplet spreading on a solid sphere, the other one is auto-ejection of liquid from a nozzle.

A. Spreading of a droplet on a solid sphere

The spreading of a droplet on the solid sphere is a classic example, and can be used to test the capacity of axisymmetric LB method in predicting the contact angle on the curve surface. For this problem (see Fig. 4), $L_r = L_z = 400$, a droplet with the radius $R = L_z/6$ is initially located at node $(r, z) = (0, L_z/3)$, the distance between the centers of droplet and sphere is k, and the radius of solid is R_s. The contact angle is θ, which can be calculated by the cosines law with the measured values of R, k, and R_s [35,40]. The no-slip boundary condition (NSBC) imposed on the left, right, and bottom boundaries, and the halfway bounce-back scheme is adopted to treat such a boundary condition [41]. In addition, the convection boundary condition (CBC) [42] is attached on the top boundary, the wetting boundary condition (WBC) is applied on the solid surface, and the symmetry boundary condition is used at the axial line $r = 0$. The initial distribution of order parameter is given by

$$\phi(z, r) = 0.5 + 0.5 \ \tanh\left[2 \ \frac{R - \sqrt{r^2 + (z - L_z/3)^2}}{W}\right]. \quad (50)$$

(a)

(b)

(c)

(d)
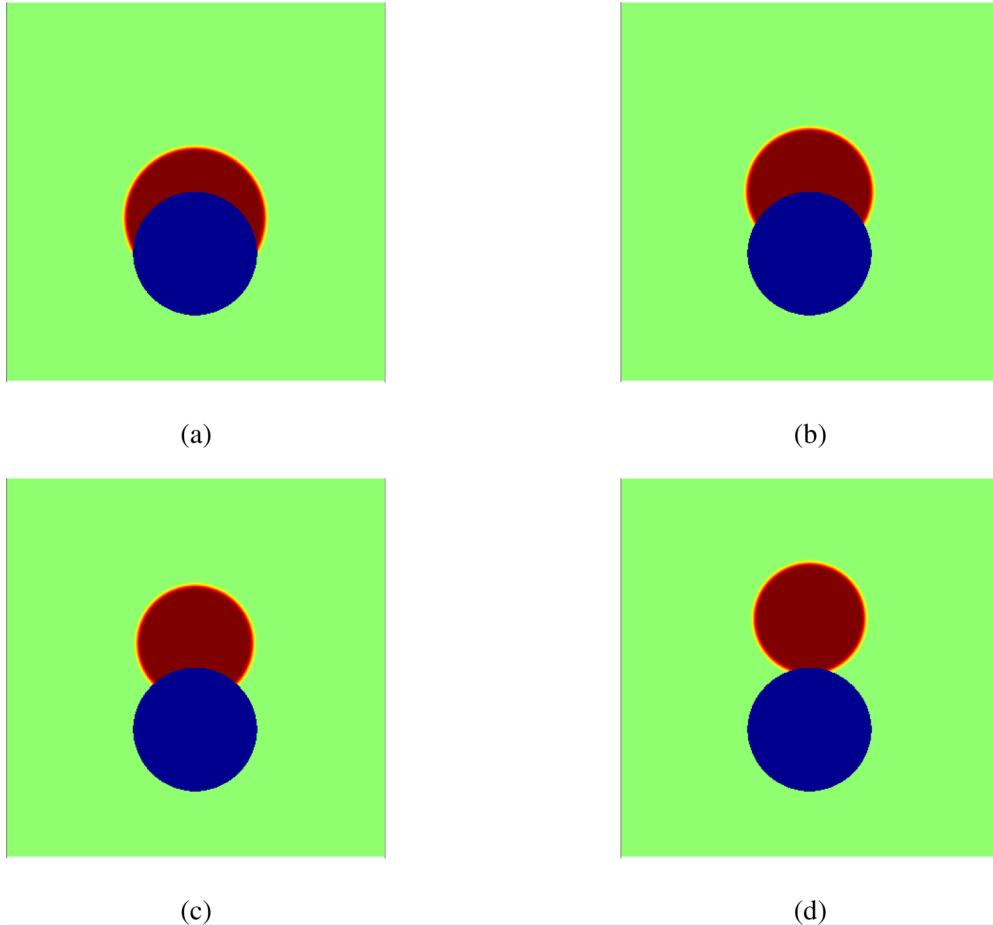
FIG. 5. The equilibrium states of the droplet obtained by the axisymmetric LB method [(a) $\theta = 30°$, (b) $\theta = 60°$, (c) $\theta = 90°$, and (d) $\theta = 120°$].

TABLE II. Units and values used in numerical simulations

Variable	Length	Mass	Time	Density	Dynamic viscosity	Surface tension coefficient
unit	Δx	mu	Δt	$mu/\Delta x^3$	$mu/\Delta x \Delta t$	$mu/\Delta t^2$
value	10^{-4} m	10^{-9} kg	10^{-5} s	10^3 kg/m^3	1 kg/ms	10 kg/s^2

In our simulations, the densities of the droplet and gas are fixed as $\rho_l = 100$ and $\rho_g = 0.1$, the dynamic viscosities of droplet and gas are $\mu_l = 1.0$ and $\mu_g = 0.01$. The surface tension coefficient is $\sigma = 0.01$, the thickness of the interface $W = 5\Delta x$ and the contact angles are specified as $\theta = 30°$, $60°$, $90°$, and $135°$. The equilibrium states of the droplet under different contact angles are presented in Fig. 5, and the predicted values of contact angle are listed in Table I. From this table, one can find that the maximum relative error between the predicted values and theoretical data is less than 3%, which indicates that the present LB method and the treatments on the boundary conditions are accurate for the axisymmetric two-phase flows.

B. Auto-Ejection of liquid from a nozzle

In the study of liquid auto-ejection, the basic lattice units and their values are listed in Table II. A grid-independence is first conducted before performing the simulation of auto-ejection, and for this purpose, the grid sizes are chosen as $N_r \times N_z = 400 \times 1400$, $N_r \times N_z = 600 \times 2100$, and $N_r \times N_z = 800 \times 2100$. The halfway bounce-back scheme is used for NSBC and no-flux boundary condition (NFBC) imposed on the left, right, and bottom boundaries, the CBC [42] is applied on the top boundary. For the nozzle wall, the halfway bounce-back scheme is used to treat the NSBC for flow field, while for phase field, the WBC is adopted. The schematic and boundary conditions of the problem are shown in Fig. 1 where the tube is located at the axial line $(r, z) = (0, 250)$, and the following initial distribution of the phase field is applied,

$$\phi(r, z) = 0.5 + 0.5 \, \tanh\left[\frac{2(300 - z)}{W}\right]. \qquad (51)$$

In this test, the geometric and material parameters are chosen based on the previous experiments [19]. The density and dynamic viscosity of the gas phase are fixed as $\rho_g = 1.2$ kg/m^3 and $\mu_g = 2 \times 10^{-5}$ kg/ms, the initial contact angle is $\theta = 0°$ and the initial interface height is $L_0 = 5$ mm. Here L_0 represents the capillary climbing under normal gravity

TABLE III. The physical parameters of PDMS fluids in simulations

Density	Kinematic viscosity	Dynamic viscosity	Surface tension coefficient
ρ_l (kg/m^3)	ν_l (cS)	σ (kg/s^2)	μ_l (kg/ms)
760	0.65	4.9×10^{-4}	0.0159
872	2.0	1.744×10^{-3}	0.0187
913	5.0	4.565×10^{-3}	0.0197

before the drop-tower experiment commences, which avoids complications at the corner [23].

The physical parameters of PDMS fluids and geometrical parameters of nozzles are listed in Tables III and IV. Due to the use of whole or half grids in this simulations, the geometrical parameters in lattice units are slightly different from those used in the experiments. We simulate the rising process of 0.65cS fluid in tube #35 [19], and present the motion of the meniscus in Fig. 6 where the numerical results are in agreement with the experimental data. In addition, we also note that the differences of imbibition height and meniscus velocity under different grid sizes are very small, thus in the following simulations, grid size with $N_r \times N_z = 400 \times 1400$ is adopted. Actually, from Fig. 6, one can also observe that initially the meniscus experiences an acceleration and adjustment under the influence of inertial force. Before forming a steady shape and constant rising speed, the meniscus oscillates several times due to the effects of the inertial force and capillary force [see points a, b, and c in Fig. 6(a) where the initial meniscus changes from flat into concave shape]. With more fluids rising into the tube, the contact line begins to move upward at a roughly steady shape and constant speed. This steady constant rising stage persists until point d, which is corresponding to the entrance of the nozzle. Once the contact line reaches the nozzle, the interface immediately deforms to adjust its orientation relative to the tapering wall of the nozzle. This deformation further generates a capillary wave that propagates radially inward, which pushes the central portion of the meniscus backward by capillarity. At this time, the meniscus velocity will be reduced to the minimum value, which is smaller than zero [see point e in Fig. 6(b)]. Then the meniscus accelerates rapidly upward, this is mainly because the momentum of the liquid column would gradually increase when it passes through a narrowing conduit. The evolutions of meniscus at points a–e are presented in Fig. 7, which corresponds to the significant oscillations and changes appeared in Fig. 6.

Next, we calculate the volume of ejected droplets during the auto-ejection process, and the entrance of #35 tube is submerged 5 mm under the PDMS fluids with different viscosities. As seen from in Fig. 8, one droplet is ejected for the 2cS and 5cS PDMS fluids, respectively. Although the droplet-ejection altitude of 2cS PDMS fluid is higher than that of 5cS PDMS fluid, the droplet volume of latter is larger than that of former. We also list the volume of ejected drop in Table V, and find that the numerical results are close to the experimental data [19]. In addition, we also show the complete ejection process of 2cS PDMS fluid in Fig. 9 where there is an agreement between the numerical and experimental results. From this figure, one can also observe that at initial time, the meniscus moves with a stable shape along the tube [see Fig. 9(b)]. When the meniscus contacts with the nozzle,

TABLE IV. The geometry parameters of nozzle (Δx).

ID Num #	Tube length L_b	Nozzle length L_t	Tube radius R_b	Nozzle radius R_t
(a) geometry parameters of experiment				
35	489.8	116.6	101.45	50.0
36	475.4	128.8	101.35	25.3
(b) geometry parameters in simulations				
35	490.0	117.0	101.5	50.0
36	476.0	129.0	101.5	25.5

however, its shape begins to change due to the capillary wave caused by the perturbation [see Fig. 9(c)]. With the increase of time, the contact line reaches the exit, a high pressure is produced by the nozzle, which makes the contact line depin from the nozzle, and a jet is formed [see Fig. 9(d)]. Then the capillary force will cause a Rayleigh breakup of the jet, which leads to the formation of droplets [see Fig. 9(e)].

V. NUMERICAL RESULTS AND DISCUSSION

In this section, we will focus on the dynamic behaviors of the interface when the meniscus advancing through the straight portion of the tube and the contracting nozzle. As we know, the meniscus velocity is determined by geometry of the nozzle, the surface tension force, the viscous force, and the gravitational force, and it changes with time and space. In the following parts, the effects of the contraction ratio $C = R_t/R_b$, the length ratio $K = L_t/L$ and the contact angle θ are considered. In our simulations, the geometric parameters are fixed as $R_b = 10$ mm, $L = 49.5$ mm, and $L_0 = 5$ mm, the physical parameters of fluid are chosen based on the experiments [19], where the fluid density and dynamic viscosity are given as $\rho_l = 913$ kg/m^3 and 0.004565 kg/ms, the surface tension coefficient $\sigma = 0.0197$ kg/s^2. To describe the motion and deformation of the meniscus, we track the velocity V_c and imbibition height H_c of the meniscus along the centerline of the tube.

A. Effect of contraction ratio

To explore the effect of contraction ratio, we conduct some simulations at different values of R_t, and plot the velocity profile and meniscus position in Fig. 10 where the time is recorded from initial moment to the droplet being formed. From this figure, one can observe that the maximum value of V_c decreases with increasing contraction ratio [Fig. 10(a)]. This is because when the contraction ratio decreases, the liquid column is accelerated more quickly. From Fig. 10(b), one can also find that the largest capillary necking height of the contact line also decreases with the increase of contraction ratio. Additionally, we plotted the changes of maximum velocity V_{max} and maximum height under different values of the contraction ratio C. As shown in Fig. 11, the maximum velocity and height decrease with the increase of C.

To see the dynamic process more clearly, we also plot the evolutions of flow field and interface of the cases $C = 0.25$, 0.275, and 0.37 in Figs. 12–14 where the point e is taken as the start point of the ejection process, and the record time is $t^* = t - t_e$. At $t^* = 0$ s, the contact line is subjected to the radial capillary wave, and the interface depresses to the lowest position. After an acceleration of interface passing through the nozzle, the contact line reaches the nozzle exit ($t^* = 0.165$ s) where the velocity reaches the maximum value. Then a high pressure will push central portion of the meniscus out of the nozzle lip, and a jet is formed ($t^* = 0.26$ s). Under the effect of surface tension force, the capillary necking commences on
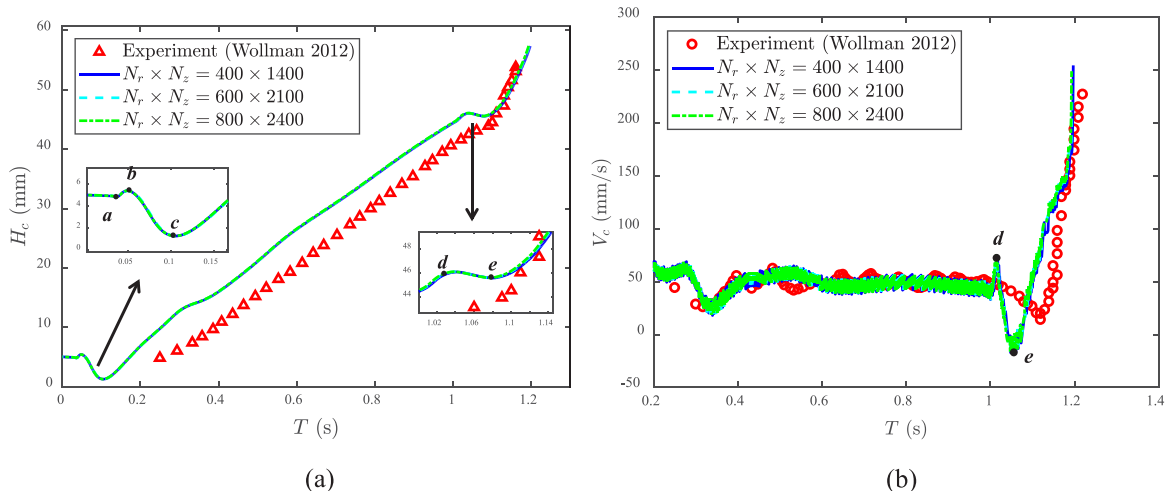
FIG. 6. The imbibition height and meniscus velocity along the centerline of the tube #35 [(a) the position of meniscus, (b) the velocity of the meniscus].
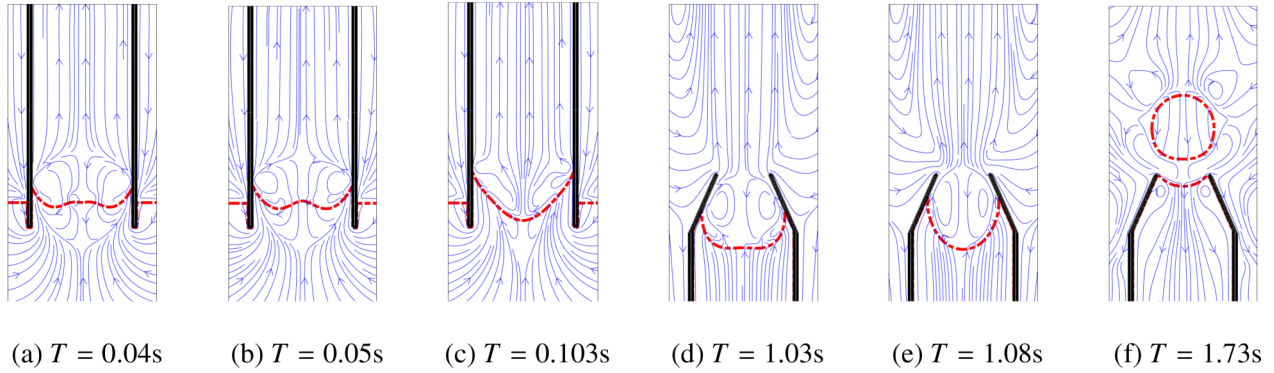
(a) $T = 0.04$s   (b) $T = 0.05$s   (c) $T = 0.103$s   (d) $T = 1.03$s   (e) $T = 1.08$s   (f) $T = 1.73$s

FIG. 7. The evolutions of meniscus at specific time stage in tube #35 [(a) point a, (b) point b, (c) point c, (d) point d, (e) point e, (f) after point e].

the jet, a droplet begins to pinch off at the tip (see Fig. 12 at $t^* = 0.31$ s). Finally, a droplet separates from the liquid neck, and the liquid column slowly shrinks back to the lip of the nozzle (see Figs. 12 and 13 at $t^* = 0.36$ s). Different from the cases of $C = 0.25$ and 0.275, the capillary necking and droplet pinch off do not occur for the case of $C = 0.37$ due to a lower kinetic energy when $t^* \geqslant 0.31$ s [see Fig. 14(d)], while the contact line begins to retract until moving back to the nozzle end [see Fig. 14(e)].

B. Effect of length ratio

We now consider effect of the length ratio $K = L_t/L$ on the ejection process in Fig. 15 where $K = 0.09, 0.15, 0.21$ and the contraction ratio $C = 0.25$. As seen from this figure, the maximum value of V_c increases with the decrease of K. For a small $K = 0.09$ with $\alpha = 59.03°$, the contraction obstructs much of the upward momentum of the liquid column, and the acceleration process becomes shorter due to a small nozzle length. Thus, the maximum value of V_c is smaller than that of the case $K = 0.21$ ($\alpha = 35.53°$). In a word, too gentle a contraction does not provide sufficient flow focusing to produce a long jet, while an abrupt contraction stifles the momentum of the liquid column. To clearly show the influence of length ratio, we plotted the variations of maximum velocity $V_{\max}$ and maximum height $H_{\max}$ in Fig. 16. As seen from this figure,
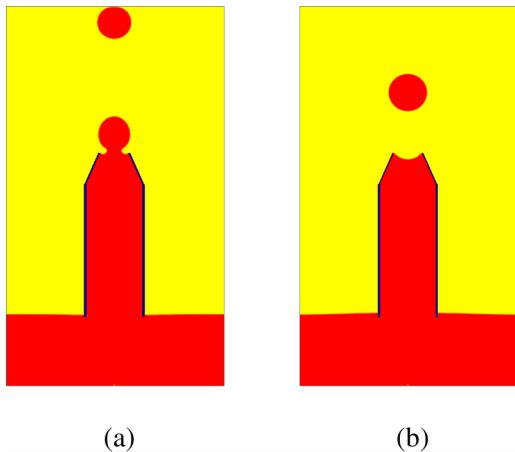
the maximum velocity and maximum height increase with increasing K.

The dynamic processes are depicted in Figs. 17 and 18, from which one can observe that after the meniscus enters the nozzle, the sudden change in curvature leads to a capillary wave propagating radially inward. Since capillarity cannot keep up with the rapid contact-line movement, the meniscus deviates markedly from a spherical shape, and a deep depression forms in the center region ($t^* = 0$ s). Then, the contractive wall leads to an acceleration of the meniscus velocity. Afterwards, the strong radial flow converges toward the center ($t^* = 0.17$ s), and surface tension makes the deeply curved interface concave rapidly. These two effects produce a high pressure and a nonuniform velocity profile at the nozzle exit, which promotes a jet ($t^* = 0.31$ s). The capillary necking first occurs at the upper end of the liquid column, and the first droplet generates gradually. After the ejection of one droplet, the jet grows a bulb at the tip while forming a neck at the base ($t^* = 0.35$ s). Shortly afterwards, the neck pinches off and the bulb detaches, producing a smaller drop ($t^* = 0.36$ s).

C. Effect of contact angle

As an important factor, the contact angle also plays a significant role on the process of droplet ejection. Different from the analysis on the effect of contact-line depinning [23], we focus on the change of surface energy caused by the contact angle. Here we take $L_t = 10.5$ mm as an example, the contraction ratio is chosen as $C = 0.25$, and the contact angles are $\theta = 0°, \theta = 10°$, and $\theta = 15°$. Figure 19 depicts the effect of contact angle on the velocity and position of meniscus. As seen from Fig. 19(a), when the meniscus rises steadily in a straight tube, the differences of velocity V_c are small for the contact angles considered here, however, the contact line reaches the nozzle earlier for the case $\theta = 0°$. As the contact line arrives at entrance of the nozzle, the meniscus begins

(a)   (b)

FIG. 8. The ejected droplets of different PDMS fluids in tube #35 [(a) 2cS PDMS fluid, (b) 5cS PDMS fluid].

TABLE V. Ejected droplets of different PDMS fluids in tube #35.

Viscosity (cS)	Volume (ml)	
	Present	Experiment
2	1.07	1.21–1.36
5	1.56	1.43–2.33

(a) $t = 0$ s

(b) $t = 0.8$ s

(c) $t = 0.99$ s

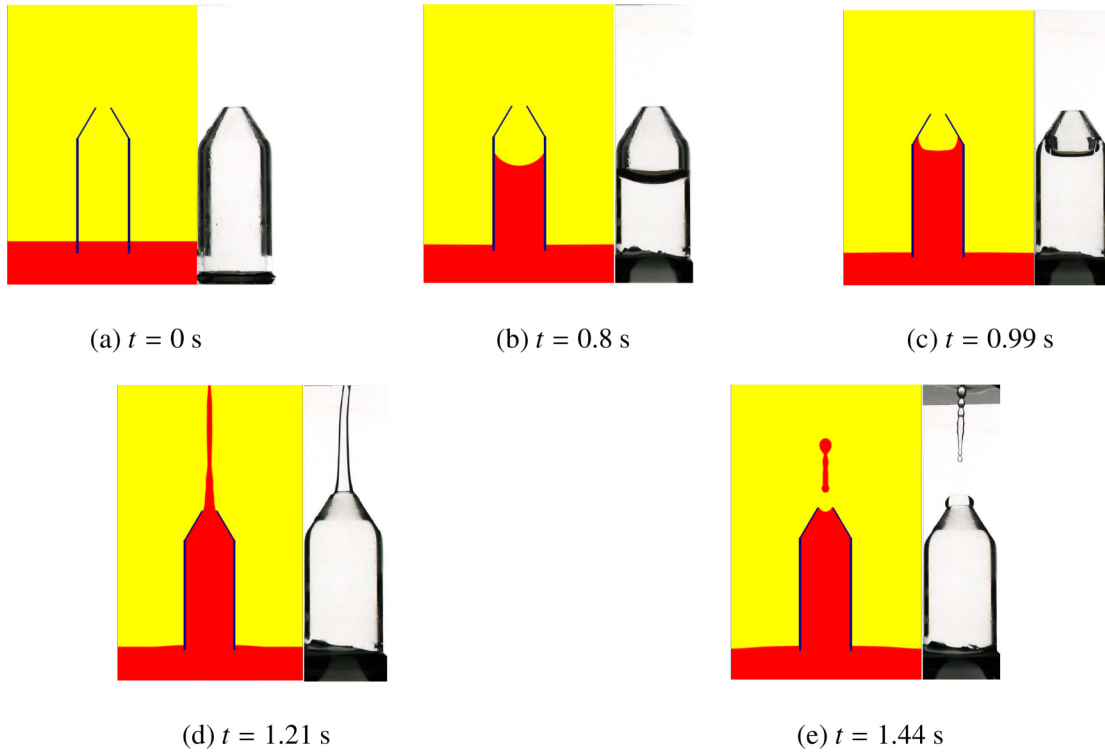(d) $t = 1.21$ s

(e) $t = 1.44$ s

FIG. 9. The auto-ejection process of 2cS PDMS fluid in tube #36 (left: numerical results, right: experimental results [19]).

to deform and depress, the velocity V_c becomes smallest. After advancing through the nozzle, the velocity has been accelerated to a maximum value, and the maximum velocity of meniscus and Weber number of the case $\theta = 15°$ is larger than those of the case $\theta = 0°$. However, for the case $\theta = 15°$, it takes longer time for the meniscus to reach the entrance of the nozzle, as shown in Fig. 19(b). This is because a larger contact angle offsets the influence of the radial capillary wave, which is caused by the slope of the nozzle. On the other hand, with the combined effect of an increasing contact angle θ and the contraction angle α, the adhesion of the contact line to nozzle is enhanced. As a result, the imbibition height

of the meniscus of the case of $\theta = 15°$ is lower. To see the effect of contact angle more clearly, we plotted the changes of maximum velocity V_{max} and maximum height H_{max} under different contact angles θ in Fig. 20. As shown in this figure, the maximum velocity first increases to maximum value, and then decreases with increasing θ, while the maximum height decreases with the increase of θ. Although the combining effect will lead to a higher Weber number when $\theta = 20°$, however, the surface energy becomes smaller and cannot provide higher kinetic energy with a larger velocity. We also present the flow fields and interfaces at two different contact angles in Figs. 21 and 22 in which some differences are also observed.

(a)

(b)
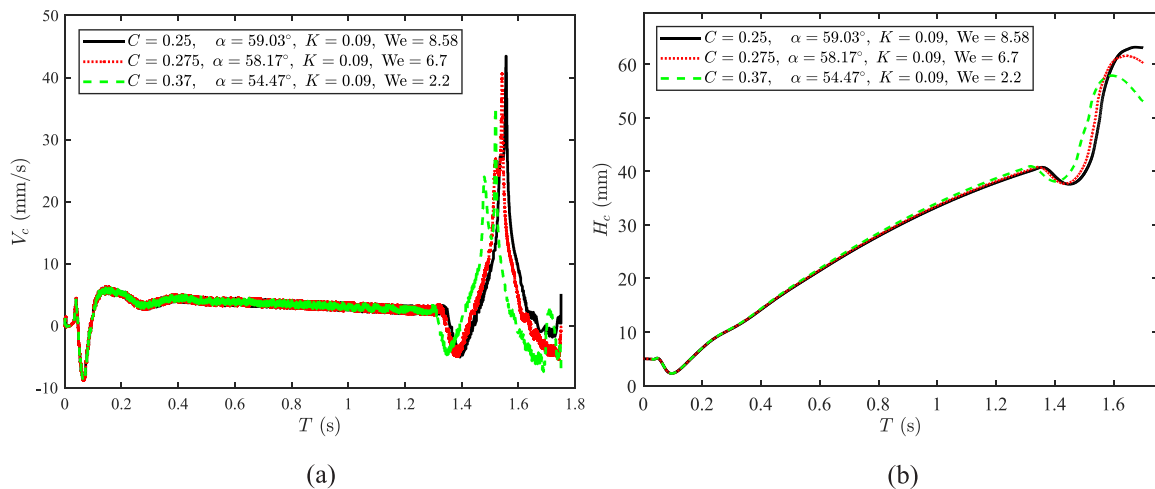
FIG. 10. The meniscus velocities along the centerline and imbibition heights at different contraction ratios [(a) meniscus velocity, (b) meniscus position].
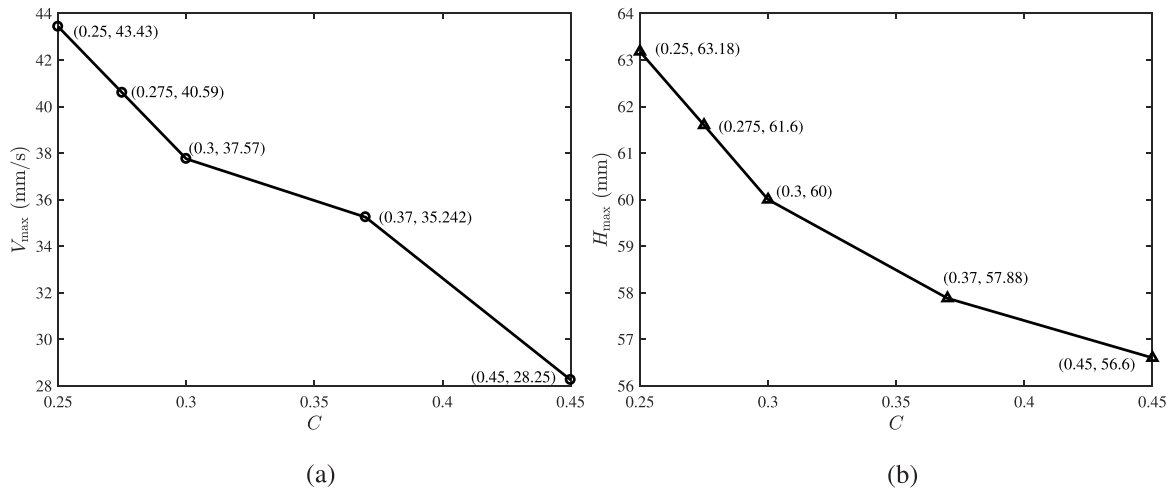
FIG. 11. The maximum velocities and heights under different contraction ratios.
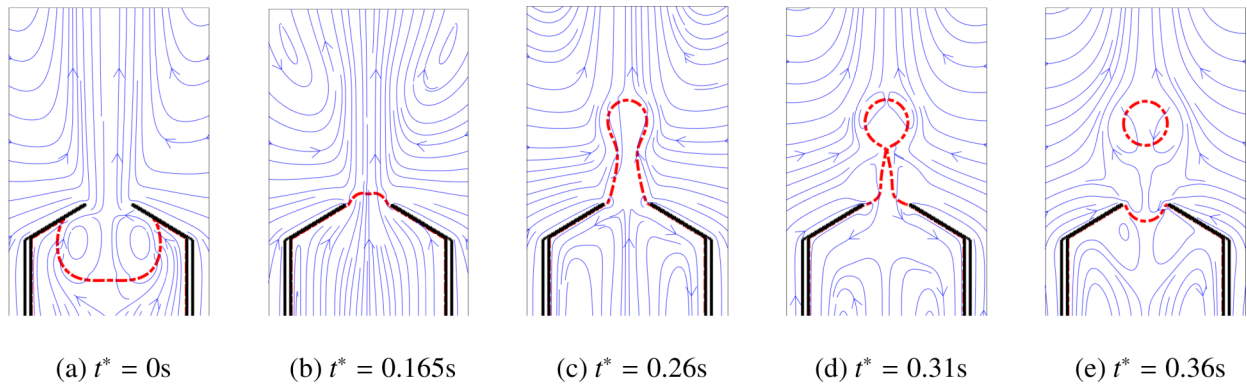
(a) $t^* = 0$s (b) $t^* = 0.165$s (c) $t^* = 0.26$s (d) $t^* = 0.31$s (e) $t^* = 0.36$s

FIG. 12. The evolutions of flow field and interface of the case with $L_t = 4.5$ mm and $C = 0.25$.

(a) $t^* = 0$s (b) $t^* = 0.16$s (c) $t^* = 0.26$s (d) $t^* = 0.31$s (e) $t^* = 0.36$s
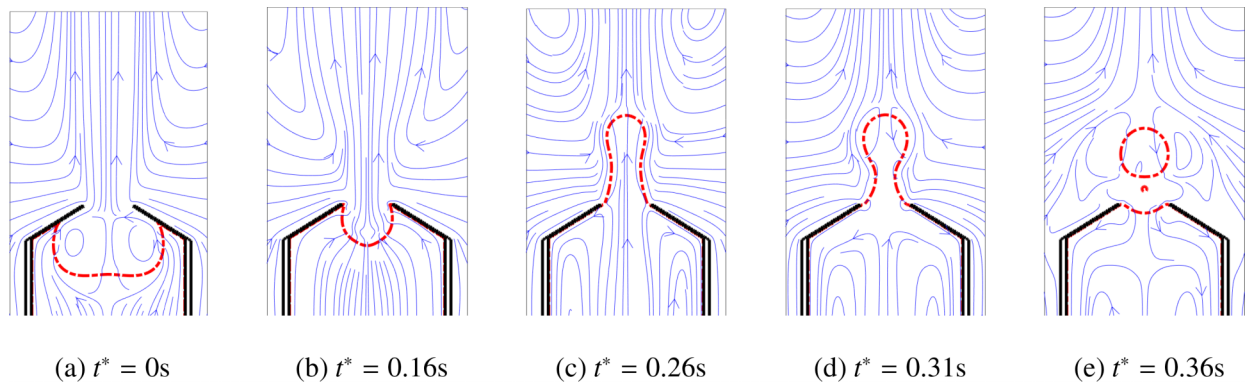
FIG. 13. The evolutions of flow field and interface of the case with $L_t = 4.5$ mm and $C = 0.275$.

(a) $t^* = 0$s   (b) $t^* = 0.17$s   (c) $t^* = 0.26$s   (d) $t^* = 0.31$s   (e) $t^* = 0.36$s
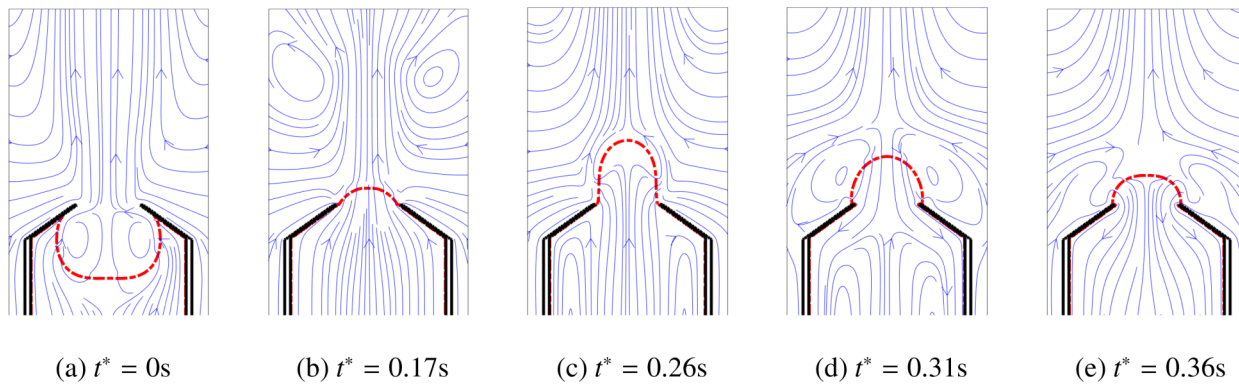
FIG. 14. The evolutions of flow field and interface of the case with $L_t = 4.5$ mm and $C = 0.37$.

(a)

(b)
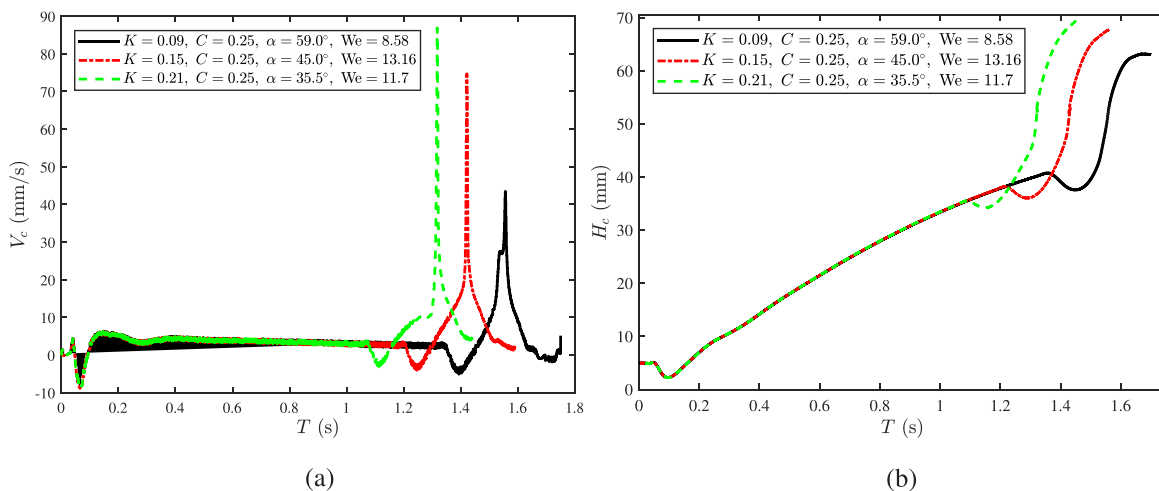
FIG. 15. The velocity profiles and imbibition heights of the cases with $K = 0.09$, $K = 0.15$, and $K = 0.21$.

(a)

(b)
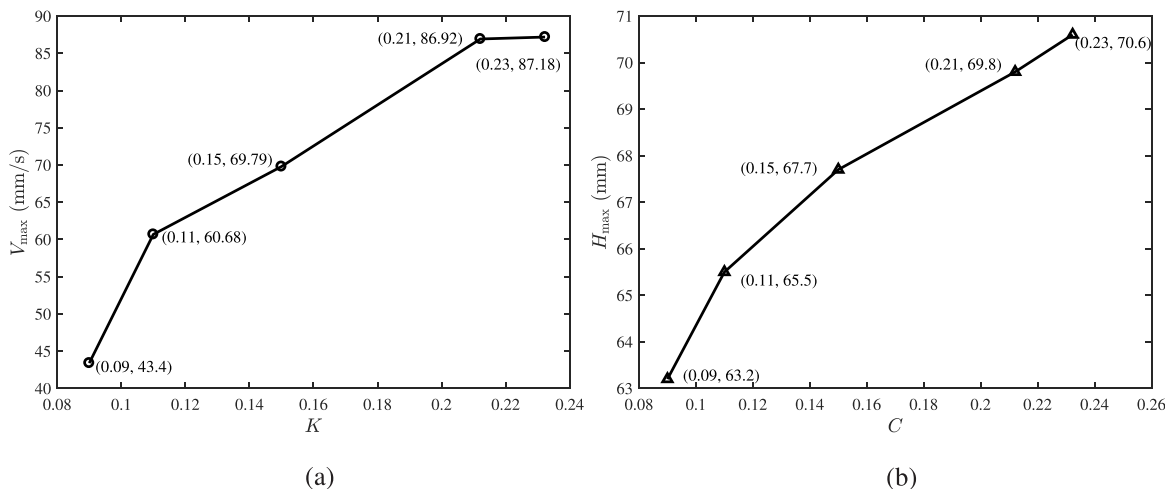
FIG. 16. The maximum velocities and heights under different length ratios.

(a) $t^* = 0$s (b) $t^* = 0.17$s (c) $t^* = 0.31$s (d) $t^* = 0.35$s (e) $t^* = 0.36$s
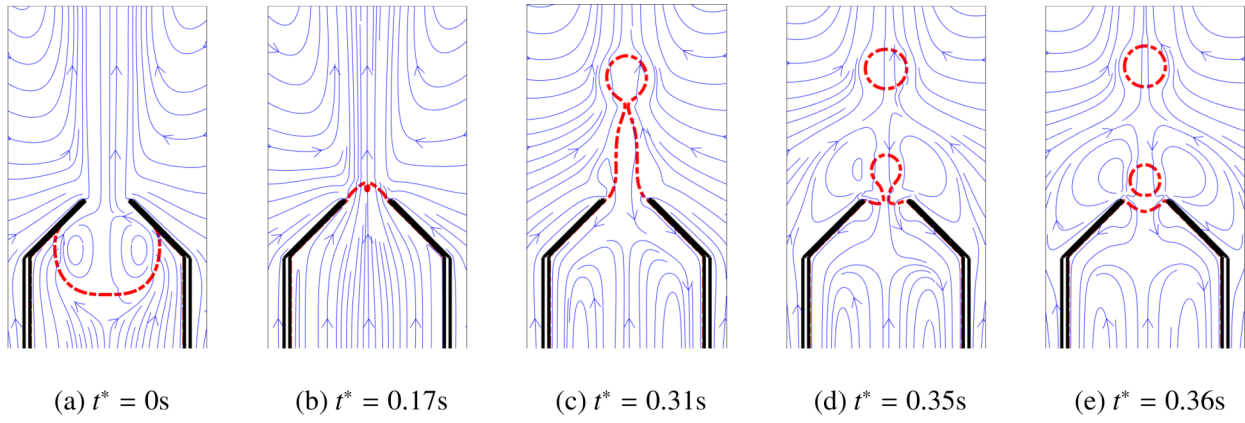
FIG. 17. The evolutions of flow field and interface of the case with $L_t = 7.5$ mm and $C = 0.25$.

(a) $t^* = 0$s (b) $t^* = 0.208$s (c) $t^* = 0.35$s (d) $t^* = 0.39$s (e) $t^* = 0.42$s
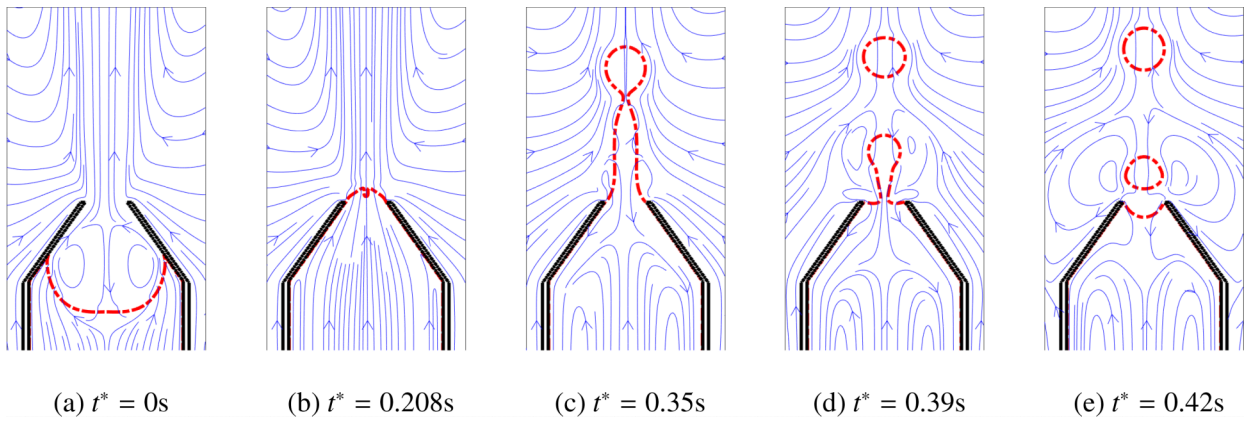
FIG. 18. The evolutions of flow field and interface of the case with $L_t = 10.5$ mm and $C = 0.25$.

(a)

(b)
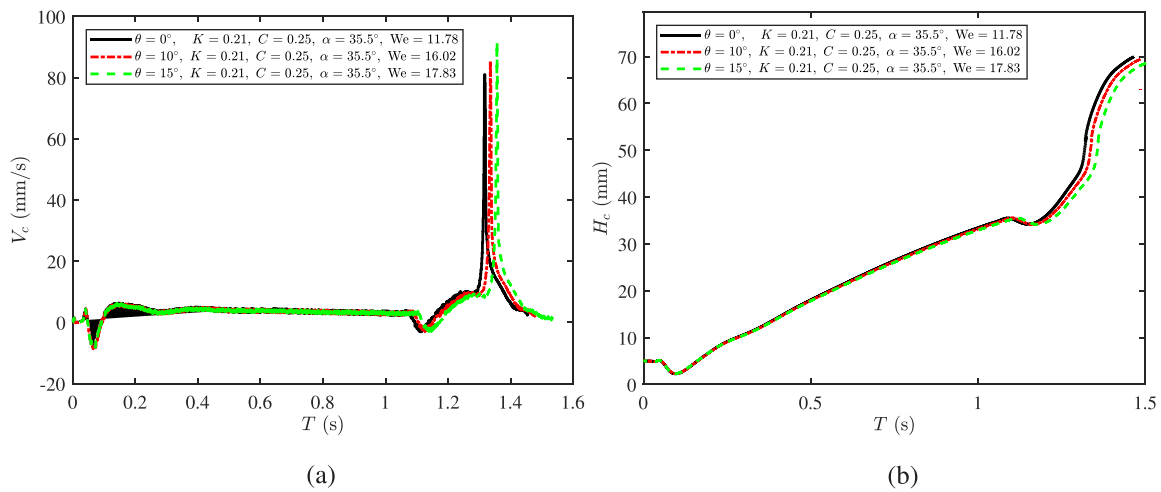
FIG. 19. The meniscus velocities along the centerline and the imbibition heights under different values of contact angle [(a) meniscus velocity, (b) imbibition height].

(a)

(b)
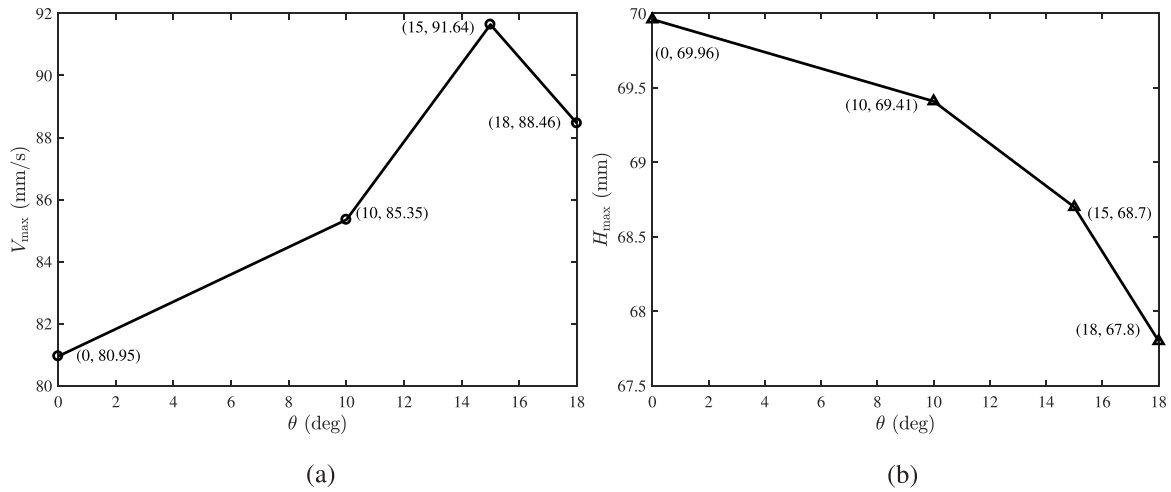
FIG. 20. The maximum velocities and heights under the different contact angles.

(a) $t^* = 0$s   (b) $t^* = 0.22$s   (c) $t^* = 0.35$s   (d) $t^* = 0.39$s   (e) $t^* = 0.42$s
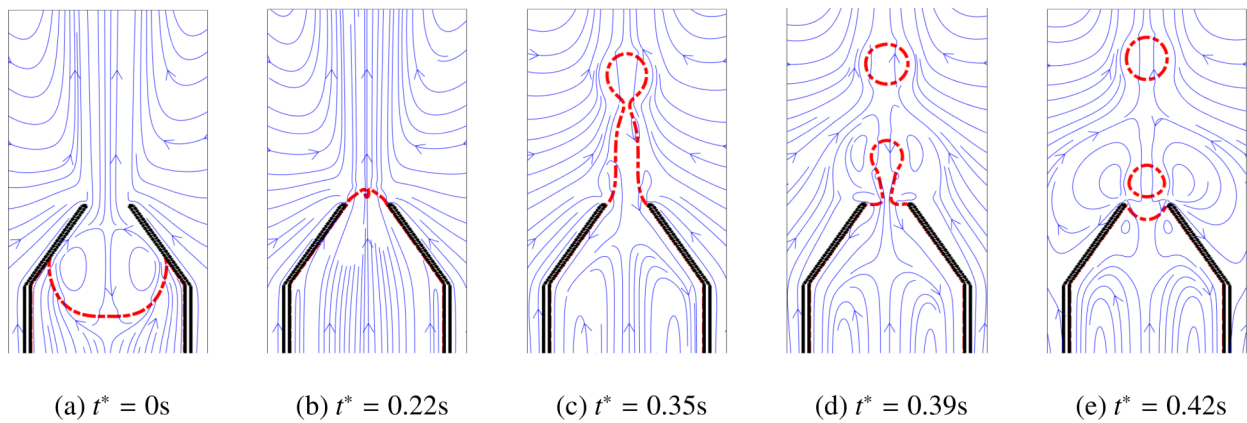
FIG. 21. The evolutions of flow field and interface of the case with $L_t = 10.5$ mm and $\theta = 10^\circ$.

(a) $t^* = 0$s   (b) $t^* = 0.215$s   (c) $t^* = 0.35$s   (d) $t^* = 0.39$s   (e) $t^* = 0.42$s
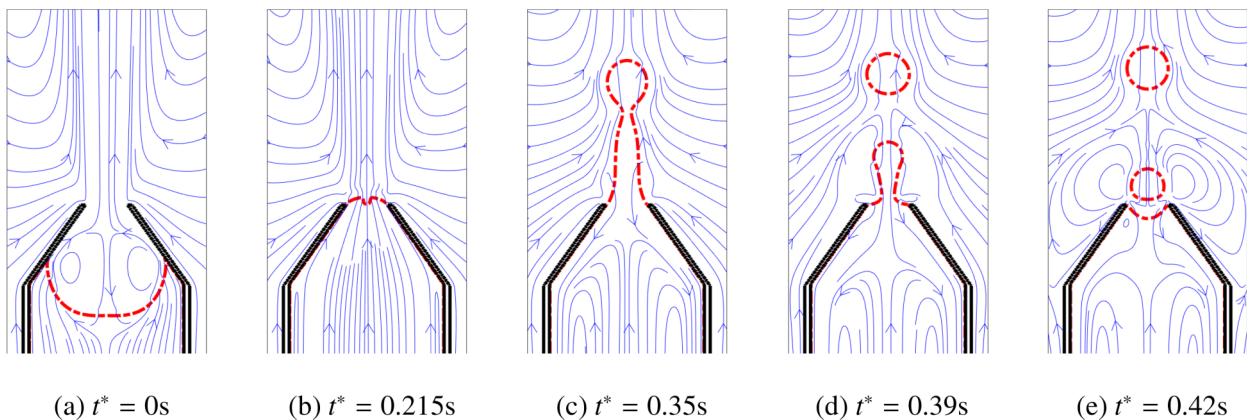
FIG. 22. The evolutions of flow field and interface of the case with $L_t = 10.5$ mm and $\theta = 15^\circ$.
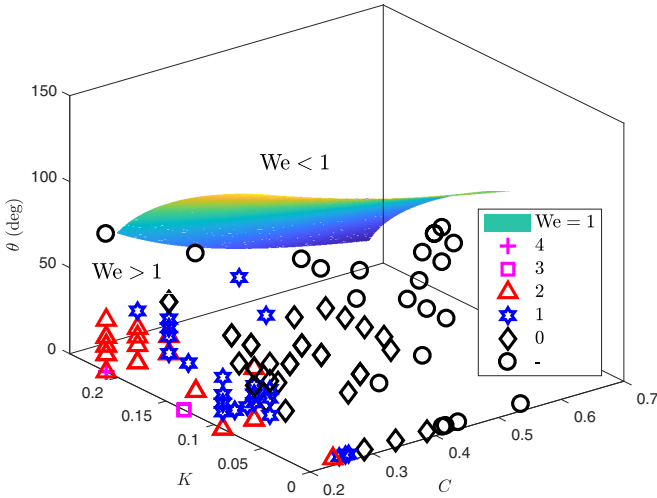
FIG. 23. The effects of length ratio (K), contraction ratio (C), and contact angle (θ) on the number of ejected droplets.

To test the critical condition [Eq. (21)], we consider the effect of contraction ratio (C), length ratio (K), and contact angle (θ) on the number of ejected droplets in Fig. 23, where the symbol $\bigcirc$ denotes the state where the interface is ejected and then oscillates around the nozzle exit. The surface We = 1 is also depicted in the picture, the value below the surface indicates We > 1 and the value above the surface is We < 1 where the contact line cannot depin from the nozzle tip. As shown in this figure, the numerical results are consistent with the theoretical prediction, and additionally, the liquid and droplets can be ejected and formed more easily under a small contraction ratio and a large length ratio.

D. Effect of nozzle structure

We now focus on the influence of nozzle structure on the ejection process, and consider three cases in Fig. 24 where the top radius R_{t_2} is fixed at 2 mm while R_{t_1} can be changed, the total length is $L = 49.5$ mm and the lengths across the nozzle are $L_{n_1} = L_{n_2} = 10$ mm. The velocity profile and meniscus position are plotted in Fig. 25 from which one can observe that there are some apparent differences between the single-

layer nozzle [Fig. 24(a)] and two-layer nozzles [Figs. 24(b) and 24(c)]. For a narrow nozzle ($R_{t_1} = 4.5$ mm) with a large structure gradient [Fig. 24(b)], the meniscus moves faster, but the maximum meniscus velocity of $R_{t_1} = 4.5$ mm is smaller than that of $R_{t_1} = 6.0$ mm [Fig. 24(a)]. However, when the radius becomes large ($R_{t_1} = 8.5$ mm) with a small gradient [Fig. 24(c)], the meniscus moves more slowly, which means that the velocity under a gentle contraction is smaller, and the maximum velocity is smaller than that of $R_{t_1} = 6.0$ mm but larger than that of $R_{t_1} = 4.5$ mm. This is because too gentle a contraction does not provide sufficient flow focusing to produce a long jet. Too abrupt a contraction stifles the momentum of the liquid column.

To analyze the structure effect more clearly, we plotted the changes of maximum velocity $V_{\max}$ and maximum height $H_{\max}$ under different radii R_{t_1} in Fig. 26. As shown in this figure, the maximum velocity and height first increase to maximum values, and then decrease with increasing R_{t_1}. And a suitable contraction will provide a sufficent kinetic energy leading to a higher instantaneous velocity when $R_{t_1} = 7.0$ mm. We also present the interfaces of three cases at $t = 1.3$ s in Fig. 27. As seen from this figure, the nozzle with $R_{t_1} = 6.0$ mm produces a higher liquid column and then two droplets forms, while the nozzle with $R_{t_1} = 8.5$ mm produces a lower liquid column and the interface moves more slowly. From the above discussion, one can find that the structure has a significant impact on the ejection process, and a desirable structure can be designed to increase the flow velocity and produce the droplets more easily.

VI. CONCLUSIONS

A comprehensive understanding of the auto-ejection process is essential for some emerging techniques, such as complicated drop generators and manipulation of small-scale flows involving drops. The auto-ejection process, however, is also very complex since it involves the interface moving, deformation, and jet breaking up. In this work, we develop a consistent and conservative axisymmetric LB method to analyze the auto-ejection process, and some distinct dynamic processes are captured. We first validate the LB method through a comparison between the numerical results and
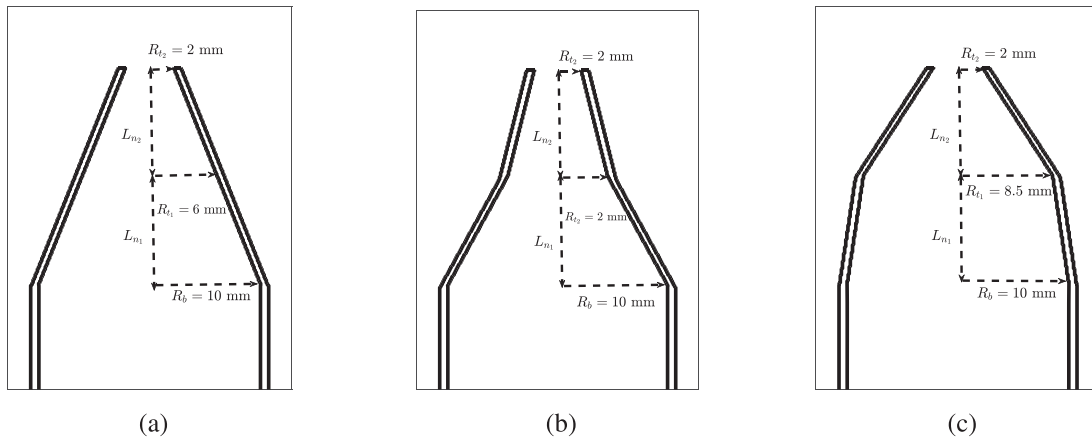

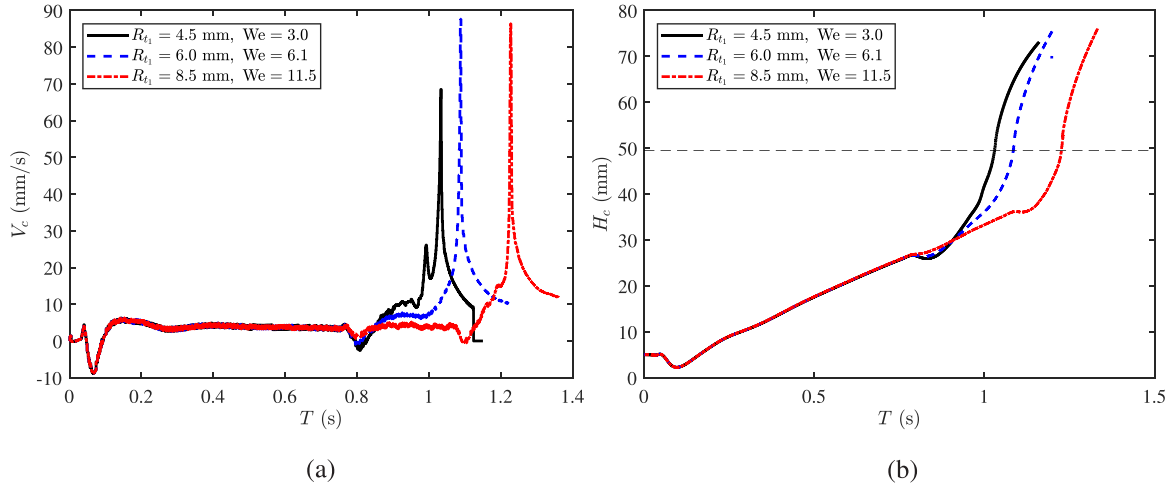FIG. 24. The schematic of different nozzle structures.

FIG. 25. The meniscus velocities along the centerline and the imbibition heights under different nozzle structures [(a) meniscus velocity, (b) meniscus velocity].

experimental data [19], and then explore the effects of nozzle geometry and fluid properties on the ejection process. Additionally, we derive an analytical solution of the meniscus velocity at the nozzle lip, and also, under the balance of inertial force and surface tension, a critical condition for ejection is obtained, which is only dependent on the liquid properties and geometric parameters. Based on the present results, the features of ejection and droplet production can be summarized as follows.

At the start of imbibition, the meniscus oscillates under the effect of inertial force. After this stage, it advances with almost a constant velocity before it reaches the entrance of nozzle. Under the disturbance of capillary wave, the meniscus velocity can reach a minimum value, which is less than zero, while it is accelerated to a maximum value after the meniscus moving through the contraction nozzle. When the contact line is pinned by the nozzle lip, a high pressure is produced from radial flow along the nozzle, which accounts for the formation of a jet. Due to the influence of surface tension, the capillary necking begins to commence on the jet, leading to a droplet pinch off.

In terms of the effect of contraction ratio $C = R_t/R_b$, we present two sets of numerical results with $L_t = 4.5$ mm and $L_t = 10.5$ mm, and find that the critical contraction ratio is about $C = 0.275$ for $L_t = 4.5$ mm, and $C = 0.315$ for $L_t = 10.5$ mm. The results also show that under a gentle contraction ratio, the liquid column cannot provide a sufficient kinetic energy, and cannot produce a long jet with forming a droplet pinch off. Additionally, when the contraction ratio is fixed, the nozzle length L_t has a significant effect on the ejection process. When L_t becomes larger, the acceleration process is longer and the liquid column will obtain more sufficient kinetic energy to create a jet, and the longer jet will also break up into more droplets.

With respect to the effect of contact angle, the results show that the maximum velocity of meniscus and Weber number increase in contact angle. However, for the case with a large contact angle, it takes longer time for the meniscus to reach the entrance of the nozzle. With an increasing contact angle and a fixed contraction angle α, the adhesion of the contact line to nozzle is enhanced. As a result, the imbibition height of the meniscus with a larger contact angle is lower, and it is
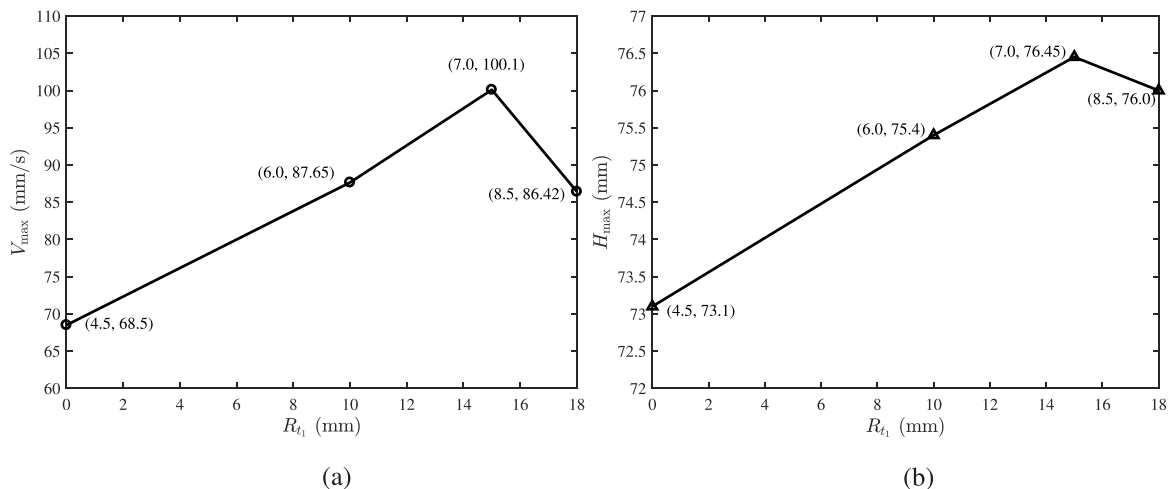

FIG. 26. The maximum velocities and heights under the different contraction radius.
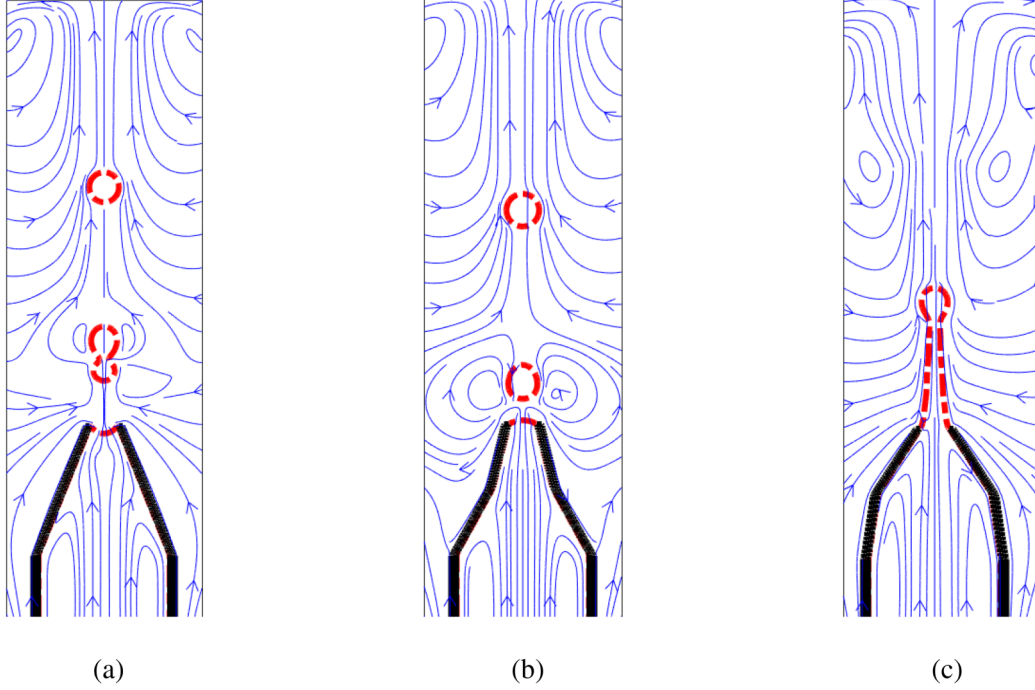
FIG. 27. The flow fields and interfaces at $t = 1.3$s [(a) $R_{t_1} = 6.0$ mm, (b) $R_{t_1} = 4.5$ mm and $R_{t_2} = 8.5$ mm].

difficult to produce droplets by capillary necking. For the effect of nozzle structure, three different types are considered. The meniscus through nozzle with a large structure gradient moves faster, but the kinetic energy of the liquid column is smaller. However, for the nozzle with a small structure gradient, the meniscus moves more slowly and induces a lower liquid column. The nozzle with a suitable gradient can be used as an accelerator for the auto-ejection process. Finally, the present work provides a guideline for the design of autonomous droplet ejector where no external force and flux are included.

APPENDIX A: DIRECT TAYLOR EXPANSION OF LB MODEL FOR THE AXISYMMETRIC ALLEN-CAHN EQUATION

1. Direct Taylor expansion

From Eqs. (30) and (30) we can obtain the moments of f_i^{eq} and F_i,

$$\sum_i f_i^{\text{eq}} = r\phi, \quad \sum_i \mathbf{c}_i f_i^{\text{eq}} = r\phi\mathbf{u} + M\phi\mathbf{E},$$

$$\sum_i \mathbf{c}_i\mathbf{c}_i f_i^{\text{eq}} = c_s^2 r\phi\mathbf{I}, \tag{A1a}$$

$$\sum_i F_i = \mathbf{0}, \quad \sum_i \mathbf{c}_i F_i = \partial_t(r\phi\mathbf{u} + M\phi\mathbf{E}) + c_s^2 r\lambda\mathbf{n}. \tag{A1b}$$

Based on the previous work [36], when the Taylor expansion is applied to Eq. (27), we have

$$\sum_{j=1}^N \frac{\Delta t^j}{j!} D_i^j f_i + O(\Delta t^{N+1})$$

$$= -\mathbf{\Lambda}_{ij}(f_j - f_j^{\text{eq}}) + \Delta t\left(\delta_{ij} - \frac{\mathbf{\Lambda}_{ij}}{2}\right)F_j, \tag{A2}$$

where $D_i = \partial_t + \mathbf{c}_i \cdot \nabla$. Introducing $f_i = f_i^{\text{eq}} + f_i^{ne}$ and substituting $f_i^{ne} = O(\Delta t)$ into Eq. (A2), one can derive the equations at first and second orders of Δt,

$$D_i f_i^{\text{eq}} = -\frac{\mathbf{\Lambda}_{ij}}{\Delta t} f_j^{ne} + \left(\delta_{ij} - \frac{\mathbf{\Lambda}_{ij}}{2}\right)F_j + O(\Delta t), \tag{A3}$$

$$D_i\left(f_i^{\text{eq}} + f_i^{ne}\right) + \frac{\Delta t}{2}D_i^2 f_i^{\text{eq}}$$

$$= -\frac{\mathbf{\Lambda}_{ij}}{\Delta t} f_j^{ne} + \left(\delta_{ij} - \frac{\mathbf{\Lambda}_{ij}}{2}\right)F_j + O(\Delta t^2). \tag{A4}$$

From Eq. (A3) we have

$$\frac{\Delta t}{2}D_i^2 f_i^{\text{eq}} = -\frac{1}{2}D_i\mathbf{\Lambda}_{ij} f_j^{ne}$$

$$+ \frac{\Delta t}{2}D_i\left(\delta_{ij} - \frac{\mathbf{\Lambda}_{ij}}{2}\right)F_j + O(\Delta t^2), \tag{A5}$$

then substituting Eq. (A5) into Eq. (A4) yields

$$
D_i f_i^{\text{eq}} + D_i\left(\delta_{ij} - \frac{\mathbf{\Lambda}_{ij}}{2}\right)f_j^{ne} + \frac{\Delta t}{2}D_i\left(\delta_{ij} - \frac{\mathbf{\Lambda}_{ij}}{2}\right)F_j
$$
$$
= -\frac{\mathbf{\Lambda}_{ij}}{\Delta t}f_j^{ne} + \left(\delta_{ij} - \frac{\mathbf{\Lambda}_{ij}}{2}\right)F_j + O(\Delta t^2). \qquad \text{(A6)}
$$

Summing Eq. (A6) over i gives rise to the following result,

$$
\partial_t \sum_i f_i^{\text{eq}} + \nabla \cdot \sum_i \mathbf{c}_i f_i^{\text{eq}} + \partial_t \sum_i \left(\delta_{ij} - \frac{\mathbf{\Lambda}_{ij}}{2}\right)f_j^{ne}
$$
$$
+ \nabla \cdot \sum_i \mathbf{c}_i\left(\delta_{ij} - \frac{\mathbf{\Lambda}_{ij}}{2}\right)f_j^{ne}
$$
$$
+ \frac{\Delta t}{2}\partial_t \sum_i \left(\delta_{ij} - \frac{\mathbf{\Lambda}_{ij}}{2}\right)F_j
$$
$$
+ \frac{\Delta t}{2}\nabla \cdot \sum_i \mathbf{c}_i\left(\delta_{ij} - \frac{\mathbf{\Lambda}_{ij}}{2}\right)F_j
$$
$$
= -\frac{1}{\Delta t}\sum_i \mathbf{\Lambda}_{ij}f_j^{ne} + \sum_i \left(\delta_{ij} - \frac{\mathbf{\Lambda}_{ij}}{2}\right)F_j. \qquad \text{(A7)}
$$

In addition, from Eq. (A3) we also have

$$
\sum_j \mathbf{c}_j f_j^{ne} = -\frac{\Delta t}{s_3^f}[\partial_t(r\phi\mathbf{u} + M\phi\mathbf{E})
$$
$$
+ \nabla \cdot c_s^2 r\phi\mathbf{I} - \left(1 - \frac{s_3^f}{2}\right)\sum_j \mathbf{c}_j F_j\Bigg], \qquad \text{(A8)}
$$

substituting Eq. (A8) into Eq. (A7) and with the help of the moments of f_i and F_i, one can derive the axisymmetric Allen-Cahn equation [Eq. (22)] with $M_\phi = c_s^2(\tau_f - 0.5)\Delta t$ ($1/\tau_f = s_3^f = s_5^f$).

APPENDIX B: DIRECT TAYLOR EXPANSION OF LB MODEL FOR CONSISTENT NAVIER-STOKES EQUATIONS

1. Direct Taylor expansion

Similarly, we can obtain the moments of g_i^{eq} and G_i from Eqs. (35) and (38),

$$
\sum_i g_i^{\text{eq}} = \mathbf{0}, \quad \sum_i \mathbf{c}_i g_i^{\text{eq}} = r\rho\mathbf{u},
$$

$$
\sum_i \mathbf{c}_i\mathbf{c}_i g_i^{\text{eq}} = r\rho\mathbf{u}\mathbf{u} + rp\mathbf{I} + \frac{\mathbf{m}^\phi\mathbf{u} + \mathbf{u}\mathbf{m}^\phi}{2},
$$

$$
\sum_i \mathbf{c}_i\mathbf{c}_i\mathbf{c}_i g_i^{\text{eq}} = r\rho c_s^2 \Delta \cdot \mathbf{u}, \qquad \text{(B1a)}
$$

$$
\sum_i G_i = r\mathbf{u}\cdot\nabla\rho, \quad \sum_i \mathbf{c}_i G_i = \bar{\mathbf{F}}, \quad \sum_i \mathbf{c}_i\mathbf{c}_i G_i = \mathbf{M}_{2,G}. \qquad \text{(B1b)}
$$

Besides, one can also determine the moments of the nonequilibrium distribution function g_i^{ne},

$$
\sum_i g_i^{ne} = -\frac{\Delta t}{2}r\mathbf{u}\cdot\nabla\rho, \quad \sum_i \mathbf{c}_i g_i^{ne} = -\frac{\Delta t}{2}\bar{\mathbf{F}}. \qquad \text{(B1c)}
$$

Similar to the analysis on the LB model for axisymmetric Allen-Cahn equation, the equations at the first and second orders of Δt can be expressed as

$$
D_i g_i^{\text{eq}} = -\frac{\mathbf{\Lambda}_{ij}}{\Delta t}g_j^{ne} + \left(\delta_{ij} - \frac{\mathbf{\Lambda}_{ij}}{2}\right)G_j + O(\Delta t), \qquad \text{(B2)}
$$

$$
D_i g_i^{\text{eq}} + D_i\left(\delta_{ij} - \frac{\mathbf{\Lambda}_{ij}}{2}\right)g_j^{ne} + \frac{\Delta t}{2}D_i\left(\delta_{ij} - \frac{\mathbf{\Lambda}_{ij}}{2}\right)G_j = -\frac{\mathbf{\Lambda}_{ij}}{\Delta t}g_j^{ne} + \left(\delta_{ij} - \frac{\mathbf{\Lambda}_{ij}}{2}\right)G_j + O(\Delta t^2). \qquad \text{(B3)}
$$

Summing Eq. (B2) over i and combining with the moments of g_i^{eq} and G_i, one can derive

$$
\partial_t \sum_i g_i^{\text{eq}} + \nabla \cdot \sum_i \mathbf{c}_i g_i^{\text{eq}} = -\frac{1}{\Delta t}\sum_i \mathbf{\Lambda}_{ij}g_j^{\text{eq}} + \sum_i \left(\delta_{ij} - \frac{\mathbf{\Lambda}_{ij}}{2}\right)G_j, \qquad \text{(B4a)}
$$

$$
\nabla \cdot (r\mathbf{u}) = 0. \qquad \text{(B4b)}
$$

Multiplying $\mathbf{c}_i$ on both sides of Eq. (B3), and through a summation over i, we have

$$
\partial_t \sum_i \mathbf{c}_i g_i^{\text{eq}} + \nabla \cdot \sum_i \mathbf{c}_i\mathbf{c}_i g_i^{\text{eq}} + \partial_t \sum_i \mathbf{c}_i\left(\delta_{ij} - \frac{\mathbf{\Lambda}_{ij}}{2}\right)g_j^{ne} + \nabla \cdot \sum_i \mathbf{c}_i\mathbf{c}_i\left(\delta_{ij} - \frac{\mathbf{\Lambda}_{ij}}{2}\right)g_j^{ne} + \frac{\Delta t}{2}\partial_t \sum_i \mathbf{c}_i\left(\delta_{ij} - \frac{\mathbf{\Lambda}_{ij}}{2}\right)G_j
$$
$$
+ \frac{\Delta t}{2}\nabla \cdot \sum_i \mathbf{c}_i\mathbf{c}_i\left(\delta_{ij} - \frac{\mathbf{\Lambda}_{ij}}{2}\right)G_j = -\frac{1}{\Delta t}\sum_i \mathbf{c}_i\mathbf{\Lambda}_{ij}g_j^{ne} + \sum_i \mathbf{c}_i\left(\delta_{ij} - \frac{\mathbf{\Lambda}_{ij}}{2}\right)G_j, \qquad \text{(B5)}
$$

which leads to following equation,

$$\partial_t(r\rho\mathbf{u}) + \nabla \cdot \left(r\rho\mathbf{u}\mathbf{u} + rp\mathbf{I} + \frac{\mathbf{m}^\phi\mathbf{u} + \mathbf{u}\mathbf{m}^\phi}{2}\right) + \nabla \cdot \left(1 - \frac{s_7^g}{2}\right)\left(\sum_j \mathbf{c}_j\mathbf{c}_j g_j^{ne} + \frac{\Delta t}{2}\mathbf{M}_{2,G}\right) = \bar{\mathbf{F}}. \tag{B6}$$

Now let us give an evaluation to the term $\sum_i \mathbf{c}_i\mathbf{c}_i g_i^{ne}$. Actually, from Eq. (B2) we have

$$\sum_i \mathbf{c}_i\mathbf{c}_i g_i^{ne} = -\Delta t \sum_i \mathbf{c}_i\mathbf{c}_i \mathbf{\Lambda}_{ij}^{-1}\left[D_j g_j^{eq} - \left(\delta_{ij} - \frac{\mathbf{\Lambda}_{ij}}{2}\right)G_j\right]$$

$$= -\frac{\Delta t}{s_7^g}\left[\partial_t \sum_j \mathbf{c}_i\mathbf{c}_i g_i^{eq} + \nabla \cdot \sum_i \mathbf{c}_i\mathbf{c}_i\mathbf{c}_i g_i^{eq}\right.$$

$$\left. - \left(1 - \frac{s_7^g}{2}\right)\mathbf{M}_{2,G}\right]$$

$$= -\frac{\Delta t}{s_7^g}c_s^2 r\rho\left(\nabla\mathbf{u} + \nabla\mathbf{u}^\top\right)$$

$$- \frac{\Delta t}{s_7^g}\left[\partial_t\left(r\rho\mathbf{u}\mathbf{u} + rp\mathbf{I} + \frac{\mathbf{m}^\phi\mathbf{u} + \mathbf{u}\mathbf{m}^\phi}{2}\right)\right.$$

$$\left. + c_s^2\mathbf{u}\nabla(r\rho) + c_s^2\nabla(r\rho)\mathbf{u}\right]$$

$$- \frac{\Delta t}{s_7^g}\left[c_s^2(\rho\nabla \cdot r\mathbf{u} + r\mathbf{u} \cdot \nabla\rho)\mathbf{I}\right.$$

$$\left. - \left(1 - \frac{s_7^g}{2}\right)\mathbf{M}_{2,G}\right]. \tag{B7}$$

Additionally, the term $\partial_t(r\rho\mathbf{u}_\alpha\mathbf{u}_\beta)$ can be evaluated by

$$\partial_t(r\rho\mathbf{u}_\alpha\mathbf{u}_\beta) = 2\partial_t(r\rho\mathbf{u}_\alpha\mathbf{u}_\beta) - \partial_t(r\rho\mathbf{u}_\alpha\mathbf{u}_\beta)$$

$$= \mathbf{u}_\alpha\bar{\mathbf{F}}_\beta + \bar{\mathbf{F}}_\alpha\mathbf{u}_\beta - \mathbf{u}_\alpha\nabla_\beta r\rho\mathbf{u}_\alpha\mathbf{u}_\beta - \mathbf{u}_\alpha\nabla_\beta rp\delta_{\alpha\beta}$$

$$- \mathbf{u}_\alpha\nabla_\beta\mathbf{m}_\alpha^{\phi c}\mathbf{u}_\beta$$

$$- \mathbf{u}_\beta\nabla_\alpha r\rho\mathbf{u}_\alpha\mathbf{u}_\beta - \mathbf{u}_\beta\nabla_\alpha rp\delta_{\alpha\beta} - \mathbf{u}_\beta\nabla_\alpha\mathbf{m}_\beta^{\phi c}\mathbf{u}_\alpha$$

$$+ r\rho\mathbf{u}_\beta\partial_t\mathbf{u}_\alpha + r\rho\mathbf{u}_\alpha\partial_t\mathbf{u}_\beta - \partial_t(r\rho\mathbf{u}_\alpha\mathbf{u}_\beta)$$

$$= \mathbf{u}_\alpha\bar{\mathbf{F}}_\beta + \bar{\mathbf{F}}_\alpha\mathbf{u}_\beta + O(Ma^2), \tag{B8}$$

then substituting Eq. (B8) into Eq. (B7) yields

$$\left(1 - \frac{s_7^g}{2}\right)\left(\sum_i \mathbf{c}_j\mathbf{c}_j g_j^{ne} + \frac{\Delta t}{2}\mathbf{M}_{2,G}\right)$$

$$= \Delta t\left(\frac{1}{2} - \frac{1}{s_7^g}\right)c_s^2 r\rho(\nabla\mathbf{u} + \nabla\mathbf{u}^\top)$$

$$+ \Delta t\left(\frac{1}{2} - \frac{1}{s_7^g}\right)(\mathbf{u}\bar{\mathbf{F}} + \bar{\mathbf{F}}\mathbf{u} + \partial_t\mathbf{m}^\phi\mathbf{u})$$

$$+ \Delta t\left(\frac{1}{2} - \frac{1}{s_7^g}\right)c_s^2[\mathbf{u}\nabla r\rho + \nabla(r\rho)\mathbf{u} + r\mathbf{u} \cdot \nabla\rho\mathbf{I}]$$

$$- \Delta t\left(\frac{1}{2} - \frac{1}{s_7^g}\right)\mathbf{M}_{2,G}, \tag{B9}$$

where $\mathbf{M}_{2,G}$ should be designed as

$$\mathbf{M}_{2,G} = \mathbf{u}\bar{\mathbf{F}} + \bar{\mathbf{F}}\mathbf{u} + \partial_t\mathbf{m}^{\phi c}\mathbf{u} + c_s^2[\mathbf{u}\nabla r\rho + \nabla(r\rho)\mathbf{u}]$$

$$+ c_s^2 r\mathbf{u}\nabla \cdot \rho\mathbf{I}$$

$$= \mathbf{u}(\bar{\mathbf{F}} + c_s^2\nabla r\rho) + (\bar{\mathbf{F}} + c_s^2\nabla r\rho)\mathbf{u} + \partial_t\mathbf{m}^{\phi c}\mathbf{u}$$

$$+ c_s^2 r\mathbf{u}\nabla \cdot \rho\mathbf{I}. \tag{B10}$$

Substituting Eqs. (B10) and (B9) into Eq. (B6), one can obtain following equation,

$$\partial_t(r\rho\mathbf{u}) + \nabla \cdot (r\rho\mathbf{u}\mathbf{u} + r\rho\mathbf{I} + \mathbf{m}^\phi\mathbf{u})$$

$$= \nabla \cdot [r\nu\rho(\nabla\mathbf{u} + \nabla\mathbf{u}^\top)] + \mathbf{F}, \tag{B11}$$

where ν is determined by Eq. (43).

APPENDIX C: COMPUTATION OF THE PRESSURE

Now let us focus on how to calculate the pressure from the distribution function g_i. According to the expression of g_0^{eq} [see Eq. (35)], we have

$$g_0(\mathbf{x}, t) - \left[g_0(\mathbf{x}, t) - g_0^{(eq)}(\mathbf{x}, t)\right]$$

$$= \frac{r(w_0 - 1)}{c_s^2}p(\mathbf{x}, t) + r\rho s_0(r, \rho, \phi, \mathbf{u}). \tag{C1}$$

Expanding $g_i(\mathbf{x} + \mathbf{c}_i\delta_t, t + \delta t)$ in Eq. (34) at position $\mathbf{x}$ and time t, one can obtain

$$\Delta t D_i g_i(\mathbf{x}, t) = -(\mathbf{M}^{-1}\mathbf{S}^g\mathbf{M})_{ij}\left[g_j(\mathbf{x}, t) - g_j^{eq}(\mathbf{x}, t)\right]$$

$$+ \Delta t\left[\mathbf{M}^{-1}\left(\mathbf{I} - \frac{\mathbf{S}^g}{2}\right)\mathbf{M}\right]_{ij}G_j(\mathbf{x}, t) + O(\Delta t^2). \tag{C2}$$

Neglecting the error term and multiply the matrix $(\mathbf{M}^{-1}\mathbf{S}^{g-1}\mathbf{M})$ on both sides of Eq. (C2), we can get

$$g_i(\mathbf{x}, t) - g_i^{eq}(\mathbf{x}, t) = -\Delta t(\mathbf{M}^{-1}\mathbf{S}^{g-1}\mathbf{M})_{ij}D_j g_j(\mathbf{x}, t)$$

$$+ \Delta t\left[(\mathbf{M}^{-1}\mathbf{S}^{g-1}\mathbf{M})_{ij} - \frac{\mathbf{I}}{2}\right]G_j(\mathbf{x}, t), \tag{C3}$$

which leads to the following result [36],

$$g_j(\mathbf{x}, t) = g_j^{(eq)}(\mathbf{x}, t) + O(\Delta t). \tag{C4}$$

With the aid of Eq. (C4), we can rewrite Eq. (C3) as

$$g_i(\mathbf{x}, t) - g_i^{\text{eq}}(\mathbf{x}, t) = -\Delta t (\mathbf{M}^{-1} \mathbf{S}^{g-1} \mathbf{M})_{ij} D_j g_j^{(\text{eq})}(\mathbf{x}, t) + \Delta t \left[(\mathbf{M}^{-1} \mathbf{S}^{g-1} \mathbf{M})_{ij} - \frac{\mathbf{I}}{2} \right] G_j(\mathbf{x}, t). \tag{C5}$$

If we substitute Eqs. (35) and (38) into Eq. (C5), and take $j = 0$, one can derive

$$g_0(\mathbf{x}, t) - g_0^{\text{eq}}(\mathbf{x}, t) = \left(\frac{3s_1^g + 2s_2^g}{3c^2 s_1^g s_2^g} \right) \Delta t \, \partial_t r p + \left(\frac{s_1^g + s_2^g}{3c^2 s_1^g s_2^g} \right) \Delta t \, \partial_t (r \rho \mathbf{u} \cdot \mathbf{u}) + \frac{s_1^g + s_2^g}{3c^2 s_1^g s_2^g} \Delta t \, \partial_t (\mathbf{m}^\phi \cdot \mathbf{u})$$

$$+ \frac{1}{9} \Delta t \frac{s_2^g - s_0^g}{s_0^g s_2^g} r \mathbf{u} \cdot \nabla \rho + \frac{2}{9} \Delta t \frac{s_1^g s_2^g - s_1^g - s_2^g}{s_1^g s_2^g} \rho u_r + \frac{1}{3c^2} \Delta t \frac{s_1^g s_2^g - s_1^g - s_2^g}{s_1^g s_2^g} \partial_t (\mathbf{m}^\phi \cdot \mathbf{u})$$

$$+ \frac{2}{3c^2} \Delta t \frac{s_1^g s_2^g - s_1^g - s_2^g}{s_1^g s_2^g} \mathbf{u} \cdot \bar{\mathbf{F}}. \tag{C6}$$

Under the incompressible condition, Eq. (C6) can be simplified by

$$g_0(\mathbf{x}, t) - g_0^{\text{eq}}(\mathbf{x}, t) = \frac{s_1^g + s_2^g}{3c^2 s_1^g s_2^g} \Delta t \, \partial_t (\mathbf{m}^\phi \cdot \mathbf{u}) + \frac{1}{9} \Delta t \frac{s_2^g - s_0^g}{s_0^g s_2^g} r \mathbf{u} \cdot \nabla \rho + \frac{2}{9} \Delta t \frac{s_1^g s_2^g - s_1^g - s_2^g}{s_1^g s_2^g} \rho u_r$$

$$+ \frac{1}{3c^2} \Delta t \frac{s_1^g s_2^g - s_1^g - s_2^g}{s_1^g s_2^g} \partial_t (\mathbf{m}^\phi \cdot \mathbf{u}) + \frac{2}{3c^2} \Delta t \frac{s_1^g s_2^g - s_1^g - s_2^g}{s_1^g s_2^g} \mathbf{u} \cdot \bar{\mathbf{F}}. \tag{C7}$$

Substituting Eq. (C7) into Eq. (C1) yields

$$\frac{r(\omega_0 - 1)}{c_s^2} p = g_0 - r \rho s_0(r, \rho, \phi, \mathbf{u}) + \frac{s_1^g + s_2^g}{3c^2 s_1^g s_2^g} \Delta t \, \partial_t (\mathbf{m}^\phi \cdot \mathbf{u}) + \frac{1}{9} \Delta t \frac{s_2^g - s_0^g}{s_0^g s_2^g} r \mathbf{u} \cdot \nabla \rho$$

$$+ \frac{2}{9} \Delta t \frac{s_1^g s_2^g - s_1^g - s_2^g}{s_1^g s_2^g} \rho u_r + \frac{1}{3c^2} \Delta t \frac{s_1^g s_2^g - s_1^g - s_2^g}{s_1^g s_2^g} \partial_t (\mathbf{m}^\phi \cdot \mathbf{u})$$

$$+ \frac{2}{3c^2} \Delta t \frac{s_1^g s_2^g - s_1^g - s_2^g}{s_1^g s_2^g} \mathbf{u} \cdot \bar{\mathbf{F}}, \tag{C8}$$

according to Eq. (B1c), g_0 can be expressed by

$$g_0 = -\frac{\Delta t}{2} r \mathbf{u} \cdot \Delta \rho - \sum_{j \neq 0} g_j. \tag{C9}$$

As a result, we can compute the hydrodynamic pressure p by

$$p = \frac{c_s^2}{(1 - \omega_0)} \left[\frac{1}{r} \sum_{i \neq 0} g_i + \frac{\Delta t}{2} \mathbf{u} \cdot \nabla \rho + \frac{1}{r} s_0(r, \rho, \phi, \mathbf{u}) + s_{p_3} \frac{\Delta t}{3r c^2} \partial_t (\mathbf{m}^\phi \cdot \mathbf{u}) + \frac{1}{9} \Delta t s_{p_2} \mathbf{u} \cdot \nabla \rho \right]$$

$$+ \frac{c_s^2}{(1 - \omega_0)} \left[\frac{2}{9r} \Delta t s_{p_1} \rho u_r + \frac{1}{3c^2 r} \Delta t s_{p_1} \partial_t (\mathbf{m}^\phi \cdot \mathbf{u}) + \frac{2}{3c^2 r} \Delta t s_{p_1} \mathbf{u} \cdot \bar{\mathbf{F}} \right], \tag{C10}$$

where $s_{p_1} = \frac{s_1^g s_2^g - s_1^g - s_2^g}{s_1^g s_2^g}$, $s_{p_2} = \frac{s_2^g - s_0^g}{s_0^g s_2^g}$, and $s_{p_3} = \frac{s_1^g + s_2^g}{s_1^g s_2^g}$.

---

[1] A. U. Chen and O. A. Basaran, A new method for significantly reducing drop radius without reducing nozzle radius in drop-on-demand drop production, Phys. Fluids **14**, L1 (2002).

[2] O. A. Basaran, Small-scale free surface flows with breakup: Drop formation and emerging applications, AIChE J. **48**, 1842 (2002).

[3] T. Goldmann and J. S. Gonzalez, Dna-printing: utilization of a standard inkjet printer for the transfer of nucleic acids to solid supports, J. Biochem. Biophys. Meth. **42**, 105 (2000).

[4] J. Cai, Y. Chen, Y. Liu, S. Li, and C. Sun, Capillary imbibition and flow of wetting liquid in irregular capillaries: A 100-year review, Adv. Colloid Interface Sci. **304**, 102654 (2022).

[5] R. Lucas, Rate of capillary ascension of liquids, Kolloid Z. **23**, 15 (1918).

[6] E. W. Washburn, The dynamics of capillary flow, Phys. Rev. **17**, 273 (1921).

[7] D. Quéré, Inertial capillarity, Europhys. Lett. **39**, 533 (1997).

[8] CH. Bosanquet, Lv. on the flow of liquids into capillary tubes, Lond. Edinb. Dublin Philos. Mag. J. Sci. **45**, 525 (1923).

[9] N. Fries and M. Dreyer, The transition from inertial to viscous flow in capillary rise, J. Colloid Interface Sci. **327**, 125 (2008).

[10] M. Hultmark, J. M. Aristoff, and H. A. Stone, The influence of the gas phase on liquid imbibition in capillary tubes, J. Fluid Mech. **678**, 600 (2011).

[11] P. L. Walls, G. Dequidt, and J. C. Bird, Capillary displacement of viscous liquids, Langmuir **32**, 3186 (2016).

[12] F. Shan, Z. Chai, and B. Shi, A theoretical study on the capillary rise of non-newtonian power-law fluids, Appl. Math. Model. **81**, 768 (2020).

[13] P.-G. De Gennes, F. Brochard-Wyart, D. Quéré, and others, *Capillarity and Wetting Phenomena: Drops, Bubbles, Pearls, Waves* (Springer, Berlin, 2004).

[14] D. Quéré, E. Raphaël, and J.-Y. Ollitrault, Rebounds in a capillary tube, Langmuir **15**, 3679 (1999).

[15] O. Shardt, P. R. Waghmare, J. J. Derksen, and S. K. Mitra, Inertial rise in short capillary tubes, RSC Adv. **4**, 14781 (2014).

[16] J. Marston, G. Toyofuku, C. Li, T. Truscott, and J. Uddin, Drainage, rebound and oscillation of a meniscus in a tube, Phys. Fluids **30**, 082103 (2018).

[17] S. Das and S. K. Mitra, Different regimes in vertical capillary filling, Phys. Rev. E **87**, 063005 (2013).

[18] É. Lorenceau, D. Quéré, J.-Y. Ollitrault, and C. Clanet, Gravitational oscillations of a liquid column in a pipe, Phys. Fluids **14**, 1985 (2002).

[19] A. P. Wollman, Capillarity-driven droplet ejection, Ph.D. thesis, Portland State University, 2012.

[20] F. Shan, J. Xiao, Z. Chai, and B. Shi, Pinning and depinning in imbibition beyond a sharp edge: A lattice boltzmann study, Int. J. Multiphase Flow **159**, 104317 (2023).

[21] A. Wollman, T. Snyder, D. Pettit, and M. Weislogel, Spontaneous capillarity-driven droplet ejection, Bull. Am. Phys. Soc. 2012.

[22] A. Wollman and M. Weislogel, New investigations in capillary fluidics using a drop tower, Exp. Fluids **54**, 1499 (2013).

[23] H. Mehrabian and J. J. Feng, Auto-ejection of liquid drops from capillary tubes, J. Fluid Mech. **752**, 670 (2014).

[24] H. Dong, W. W. Carr, and J. F. Morris, An experimental study of drop-on-demand drop formation, Phys. Fluids **18**, 072102 (2006).

[25] A. S. Utada, E. Lorenceau, D. R. Link, P. D. Kaplan, H. A. Stone, and D. Weitz, Monodisperse double emulsions generated from a microcapillary device, Science **308**, 537 (2005).

[26] V. Pekkanen, M. Mäntysalo, K. Kaija, P. Mansikkamäki, E. Kunnari, K. Laine, J. Niittynen, S. Koskinen, E. Halonen, and U. Caglar, Utilizing inkjet printing to fabricate electrical interconnections in a system-in-package, Microelectron. Eng. **87**, 2382 (2010).

[27] S. Beg, W. H. Almalki, A. Malik, M. Farhan, M. Aatif, Z. Rahman, N. K. Alruwaili, M. Alrobaian, M. Tarique, and M. Rahman, 3d printing for drug delivery and biomedical applications, Drug Discov. Today **25**, 1668 (2020).

[28] W.-B. Young, Analysis of capillary flows in non-uniform cross-sectional capillaries, Colloids Surf. A **234**, 123 (2004).

[29] M. Reyssat, L. Courbin, E. Reyssat, and H. A. Stone, Imbibition in geometries with axial variations, J. Fluid Mech. **615**, 335 (2008).

[30] B. Figliuzzi and C. R. Buie, Rise in optimized capillary channels, J. Fluid Mech. **731**, 142 (2013).

[31] J. R. Fanchi, *Principles of Applied Reservoir Simulation* (Elsevier, Amsterdam, 2005).

[32] Z. Guo, H. Han, B. Shi, and C. Zheng, Theory of the lattice boltzmann equation: Lattice boltzmann model for axisymmetric flows, Phys. Rev. E **79**, 046708 (2009).

[33] H. Liang, Y. Li, J. Chen, and J. Xu, Axisymmetric lattice boltzmann model for multiphase flows with large density ratio, Int. J. Heat Mass Transf. **130**, 1189 (2019).

[34] C. Zhan, Z. Chai, and B. Shi, Consistent and conservative phase-field-based lattice boltzmann method for incompressible two-phase flows, Phys. Rev. E **106**, 025319 (2022).

[35] X. Liu, Z. Chai, C. Zhan, B. Shi, and W. Zhang, A diffuse-domain phase-field lattice boltzmann method for two-phase flows in complex geometries, Multiscale Model. Simul. **20**, 1411 (2022).

[36] Z. Chai and B. Shi, Multiple-relaxation-time lattice boltzmann method for the navier-stokes and nonlinear convection-diffusion equations: Modeling, analysis, and elements, Phys. Rev. E **102**, 023306 (2020).

[37] D. Jacqmin, Contact-line dynamics of a diffuse fluid interface, J. Fluid Mech. **402**, 57 (2000).

[38] A. Fakhari and D. Bolster, Diffuse interface modeling of three-phase contact line dynamics on curved boundaries: A lattice boltzmann model for large density and viscosity ratios, J. Comput. Phys. **334**, 620 (2017).

[39] D. Yu, R. Mei, and W. Shyy, A unified boundary treatment in lattice boltzmann method, in *Proceedings of the 41st Aerospace Sciences Meeting and Exhibit, 6-9 January 2003, Reno, Nevada* (AIAA, Reston, VA, 2003), Paper No. AIAA 2003–953.

[40] S. Zhang, J. Tang, and H. Wu, Simplified wetting boundary scheme in phase-field lattice boltzmann model for wetting phenomena on curved boundaries, Phys. Rev. E **108**, 025303 (2023).

[41] S. Succi, *The Lattice Boltzmann Equation: for Fluid Dynamics and Beyond* (Oxford University Press, Oxford, 2001).

[42] Q. Lou, Z. Guo, and B. Shi, Evaluation of outflow boundary conditions for two-phase lattice boltzmann equation, Phys. Rev. E **87**, 063301 (2013).